ABSTRACT

Title of dissertation: REACTION FACTORIZATION
FOR DISTRIBUTED DEPOSITION SYSTEMS:
APPLICATION TO COPPER FILM GROWTH

David Arana-Chavez, Doctor of Philosophy, 2015

Dissertation directed by: Professor Raymond Adomaitis
Department of Chemical and Biomolecular Engineering

A model reduction methodology based on a Gauss-Jordan reaction factorization for thin-film deposition reaction systems is developed in this thesis. The factorization generates a transformation matrix that is used to create a new coordinate system that guides the separation of the deposition process time scales by decoupling the net-forward reaction rates to the greatest extent possible. The new coordinate space enables recasting the original model as a singular perturbation problem and consequently as a semi-explicit system of differential-algebraic equations (DAE) for the dominant dynamics in the pseudo-equilibrium limit. Additionally, the factorization reveals conserved quantities in the new reaction coordinate system as well as potential structural problems with the deposition reaction network.

The reaction factorization methodology is formulated to be suitable for application to dynamic, spatially distributed reaction systems. The factorization provides a rigorous pathway to decouple the time evolution and the spatial distributions of deposition systems when the dynamics of reactor-scale gas-phase transport are fast

relative to the deposition process. Moreover, the factorization approach provides a solution to the problem of formulating Danckwerts-type boundary conditions where gas-phase equilibrium reactions are important.

The reaction factorization is used to study the chemical vapor deposition of copper on a tubular hot-wall reactor using copper iodide as the Cu precursor. A film-growth mechanism is proposed from experimental observations that the copper films deposited on quartz substrates suggest a Volmer-Weber growth mode. A model based on this mechanism is used to track spatial distribution of the average Cu island size in the reactor.

The rate expressions used in the Cu deposition model are determined using absolute rate theory. To carry out these calculations in an organized manner, a library of object-oriented classes are created in the PYTHON programming language.

REACTION FACTORIZATION FOR DISTRIBUTED DEPOSITION SYSTEMS: APPLICATION TO COPPER FILM GROWTH

by

David Arana-Chavez

Dissertation submitted to the Faculty of the Graduate School of the
University of Maryland, College Park in partial fulfillment
of the requirements for the degree of
Doctor of Philosophy
2015

Advisory Committee:
Professor Raymond A. Adomaitis, Chair/Advisor
Professor Panagiotis Dimitrakopoulos
Professor Jeffery Klauda
Professor Michael R. Zachariah
Professor Oded Rabin

Acknowledgments

Above all I thank God for without Him nothing would be possible.

Infinite thanks to my advisor, Dr. Raymond Adomaitis (Ray), for the continuous support, patience, advice and guidance that he has given me through out these years.

Boundless thanks to my parents, David and Rosa, and my sisters, Nancy and Fabiola, for their unfailing love, sacrifice and support that helps me endure even the most difficult times. Thanks also to everyone in the UBF, my second family, for all their love and selfless help that they have always offered me.

I would also like to thank my committee members: Dr. Panagiotis Dimitrakopoulos, Dr. Michael Zachariah, Dr. Jeffrey Klauda and Dr. Oded Rabin for their insightful and valuable comments and suggestions.

I also want to thank the A. James Clark School of Engineering Fellowship for funding my first year of the doctorate program, the US National Science Foundation for providing funding for this project through grant CBET1160132, and the CONACyT (National Council of Science and Technology of Mexico) for the scholarship provided to complete my studies.

Table of Contents

List of Figures

List of Abbreviations

ϵ, δ	Perturbation parameters
ζ	Spatial dimension
t	Time
$E_{g,i}$	Band gap energy of species i
G	Net-forward reaction rate associated with a fast mode
F	Net-forward reaction rate associated with a slow mode
$[M]$	Concentration of precursor monomer
$[T]$	Concentration of precursor trimer
$[X]$	Concentration of available surface sites
$[A]$	Surface concentration of adsorbed material A
$[B]$	Concentration of bulk phase
L	Film property whose evolution is tracked during deposition simulations
K_j	Equilibrium constant for reaction j
k_j	Rate constant for reaction j
$\mathbf{c}$	Composition state vector
$\mathbf{S}$	Stoichiometric reaction coefficients matrix
$\mathbf{r}$	Net-forward reaction rates vector
n_c	Number of chemical species
n_r	Number of reaction rates
$\mathbf{U}$	Coordinate transformation matrix
$\mathbf{z}$	State vector of new coordinates associated with fast dynamic modes
$\mathbf{x}$	State vector of new coordinates associated with slow dynamic modes
$\mathbf{w}$	State vector of new coordinates associated with conserved quantities
$\mathbf{y}$	State vector of new reaction coordinates
$\mathbf{U_x}$	Row vectors of $\mathbf{U}$ corresponding to coordinates $\mathbf{x}$
$\mathbf{U_w}$	Row vectors of $\mathbf{U}$ corresponding to coordinates $\mathbf{w}$
$\mathbf{g}$	Vector with the equilibrium relationships of reversible reactions
$\mathbf{f}$	Vector of slow reaction rates
σ	Surface area to volume ratio
$\mathcal{Q}$	Equilibrium manifold
Δ_t	Size of time step used in Euler integration
J_T	Flux of trimer species in the gas phase
J_M	Flux of monomer species in the gas phase
$\mathcal{D}_\mathcal{T}$	Diffusion coefficient of the trimer species in the gas phase
$\mathcal{D}_\mathcal{M}$	Diffusion coefficient of the monomer species in the gas phase
v	Average flow velocity
$\mathbf{res}$	Vector containing the residuals of the discretized equations in Chapter 3
$\mathbf{E}$	Discretization array with collocation weights for second order derivative
$\mathbf{F}$	Discretization array with collocation weights for first order derivative
$\mathbf{F0}$	Discretization array with the weights for the first derivative at inlet
$\mathbf{F}in$	Discretization array with the weights for the first derivative at interior points
$\mathbf{F}N$	Discretization array with the weights for the first derivative at outlet
$\mathbf{E}in$	Discretization array with the weights for the second derivative at interior points
N	Number of collocation points

$\mathbf{error}$	Vector of error between solutions at different grid sizes
$\mathbf{y}_{fine}$	Results form simulations with a fine grid in Chapter 3
$\mathbf{y}_{N_i}$	Results form simulations with a grid with N_i number of collocation points
$\tau = \delta t$	Slow time scale
k_B	Boltzmann's constant
Avo	Avogadro's constant
h	Planck's constant
θ	Fractional surface coverage
η_{Cu}	Sticking coefficient of Copper on quartz substrates
η_{CuI}	Sticking coefficient of Copper Iodide on quartz substrates
r_g^{Cu}	Rate of deposition by direct impingement of Cu from the gas phase
r_g^{CuI}	Rate of deposition by direct impingement of CuI from the gas phase
r_s^{Cu}	Rate of deposition by incorporation from the edge sites
r_s^{CuI}	Rate of deposition by incorporation from the edge sites
A_g	Copper island surface area available for deposition
A_{edge}	Surface area available for deposition on the edge of a Cu island
L_{Cu}	Length of the side of a solid copper island of one atom
n_{Cu}	Number of atoms in a growing copper island
$n_{Cu_{side}}$	Number of atoms in a side of a growing copper island
L	Average islands size length (in Chapter 4)
m_{Cu}	Weight of an atom of copper
m_{CuI}	Weight of an atom of copper iodide
v_{Cu_1}	Atomic volume of copper
v_{SiO_2}	Molecular volume of SiO_2
$[\hat{X}]$	Surface site density of quartz
R_o	Inner radius of tubular reactor
A	Area perpendicular to flow direction (Chapter 4)
V_ζ	Volume of differential element of analysis
Δ_ζ	Size of spatial integration step
T	Temperature of deposition experiments
$nucSites$	Surface concentration of nucleation sites
$[Cu_3I_3]$	Gas phase concentration of copper iodide trimer
$[I_2]$	Gas phase concentration of iodine
$[Cu]$	Gas phase concentration of copper
$[Cu_2]$	Gas phase concentration of copper dimmer
$[CuI]$	Gas phase concentration of copper iodide
ξ_{el}	Energy level in electronic energy modes
ω_{el}	Degeneracy of energy level in electronic energy modes
ν	Vibrational frequency energy for vibrational energy modes
σ	Symmetry number for rotational energy modes (only in Chapter 5)
I's	Moments of inertia (Chapter 5)
ρ	Density of bulk phase materials in growing films
D_o	Bond energy between adsorbed species and surface
`trans()`	Species class method to calculate the translational partition function

`elect()`	Species class method to calculate the electronic partition function
`vibra()`	Species class method to calculate the vibrational partition function
`rota()`	Species class method to calculate the rotational partition function
`partfunc()`	Species class method to calculate partition function
`pftv()`	Method to calculate partition function without the electronic contribution
A(T,P)	Species method to estimate the Helmholtz free energy
U(T)	Species method to estimate the internal energy
H(T)	Species method to estimate the enthalpy
S(T,P)	Species method to estimate the entropy
G(T,P)	Species method to estimate the Gibbs free energy
`monoatomG`	Species class for monoatomic species in the gas phase
`polyatomG`	Species class for polyatomic species in the gas phase
`atomSurf`	Species class for surface sites
`adatom`	Species class for adsorbed atoms
`admolec`	Species class for adsorbed molecules
$\mathcal{Z}_A$	Partition function of gas-phase species A
$\mathcal{Z}_X$	Partition function of surface site X
$\mathcal{Z}_{AX}$	Partition function of adsorbed species A on site X
ν_0	Vibration frequency of the bond between the adsorbed species and the surface
ϵ_{Cu-Cu}	Adsorption energy of copper on a copper surface (only in Chapter 5)
ϵ_{Cu-SiO_2}	Adsorption energy of copper on a quartz surface (only in Chapter 5)
Δ^3	Volume of the adsorbed species
P_A	Partial pressure of gas species A (in Chapter 5)
p_{Cu}	Partial pressure of copper (in Chapter 5)
p_{Cu}^{vap}	Vapor pressure of copper (in Chapter 5)
K_{ads}^{sp}	Adsorption isotherm constant of species sp
V_p	Volume of a cubic copper island
V_{m^3}	Volume of a cubic pixel
c_{pix2m}	Scaling factor to convert pixels to length
v_{Cu}	Atomic volume of copper (in Chapter 6)
DepLen	Length of deposition zone in the CVD reactor
ρ_{Cu}	Density of copper
L_1	Length of the oxygen feed tube in the CVD reactor
L_2	Length of the zone downstream from the oxygen feed in the CVD reactor
Cu_xO	Copper oxide: cupric ($x = 1$), cuprous ($x = 2$)
DAE	Differential-Algebraic System of Equations
ODE	Ordinary Differential Equation
CVD	Chemical Vapor Deposition
MOCVD	Metal-Organic Chemical Vapor Deposition
ALD	Atomic Layer Deposition
MW	Molecular Weight
MWa	Molecular Weight of adsorbed species
MWs	Molecular Weight of surface species
CIGS	Copper Indium Gallium Sulfide

RGB	Red, green, and blue color model
scipy	Scientific python library
FCC	Face Centered Cubic crystal structure
NIST	National Institute of Standards and Technology
CCCBD	Computational Chemistry Comparison and Benchmark Database
ITO	Indium Tin Oxide
XRD	X-Ray Diffraction
RSM	Response Surface Model
kMC	kinetic Monte Carlo
MATLAB	Matrix Laboratory - Programming language developed by MathWorks
PYTHON	Programming language created by Guido van Rossum at CWI
CWI	Centrum Wiskunde & Informatica

Appendix A

M	Vector with rotameter settings
m	Scaled rotameter settings
t	Scaled temperatures
dof	Degrees of freedom
SSE	Sum of squared residuals
SST	Total sum of squares
$\mathbf{x}$	Vector with the scaled factors
n_M	Number of sets of experimental conditions
$\mathbf{Y}$	Percentage of Cu_2O on the deposited film observed experimentally
$\mathbf{y}_{RSM}$	Percentage of Cu_2O estimated by the RSM
b_0	Coefficient in the RSM determined from experimental data
$\mathbf{b}$	Vector of coefficients in the RSM determined from experimental data
$\mathbf{B}$	Matrix of coefficients in the RSM determined from experimental data
$\mathbf{c}$	Vector of coefficients of the RSM determined from experimental data
$\mathbf{X}$	Rectangular array with factor values for evaluation of the RSM
$\bar{Y}$	Mean measured value of the modeling data set
R^2	Coefficient of determination
σ_M^2	Variance of the modeling error
p	Number of identified parameters in the model
$\sigma_{b,k}^2$	Parameter variance
$s_{b,k}^2$	Approximation to the true parameter variance
t_k	Student's t-test t-value k
α	Confidence level for Student's t-test
`tinv`	MATLAB function to calculate the t-value of a given probability

Appendix B

f_i	Value of approximation of function f at collocation point i
ζ_i	Value of the spatial coordinate at collocation point i
$\Delta\zeta_{i+1}$	Spatial difference between collocation points $i+1$ and i

$\Delta\zeta_{i-1}$	Spatial difference between collocation points $i-1$ and i
ξ_i	Denominator of collocation weights at collocation point i
N	Total number of collocation points

Chapter 1

Introduction

This chapter presents the motivation to study the chemical vapor deposition (CVD) of copper and copper oxide thin films due to their current and potential applications as materials for solar energy harvesting, as well as the challenges encountered in modeling this process. A literature survey on model reduction and stiffness relaxation is also provided in the second part of this chapter.

1.1 Motivation

1.1.1 Copper and copper oxide thin films

Copper is widely used as an interconnect material in electronic circuits [1, 2] and is a key component used in absorbent layers in CIGS solar cells and photovoltaic devices [3, 4]. It has been used in metal-halide discharge lamps in the form of copper iodide [5, 6, 7], as well as a precursor, in CuI, in CVD of copper oxide thin films [8, 9].

The most common copper oxides, CuO and Cu_2O, are natural p-type semiconductors that have shown potential for photovoltaic and photoelectrochemical applications [10]. The abundance of copper and the practically null toxicity of the oxides makes Cu_xO a very attractive material for solar energy applications. Particular interest has been devoted to solar water splitting applications because the oxide bandgaps ($E_{g,Cu_2O} \approx 2.1$ eV and $E_{g,CuO} \approx 1.2$ eV) are suitable for the photo-

splitting of water to produce hydrogen and oxygen using visible light [11]. Practical application of Cu_xO to water-splitting must, however, overcome barriers such as semiconductor film instability in electrolyte solutions either by oxidation of cuprous oxide to cupric oxide [12] or by reduction of CuO to Cu_2O [10].

In the majority of the applications mentioned above, solar cells and photoelectrochemical cells, the films and electrodes are created by chemical vapor deposition (CVD) using a copper containing precursor such as [13] or by co-evaporation using elemental copper in physical vapor deposition as in [4]. Previous studies of copper oxide CVD using copper iodide as the Cu precursor [8, 9] have revealed unexpected film deposition spatial patterns: both Cu_2O and CuO deposit are found on the same substrate separated by a sharp transition between the two oxides. The abrupt change in film composition is clearly seen due to the red color of Cu_2O and black color of CuO as shown in Figure 1.1.

In earlier work [14], the temperature and oxygen partial pressure influence on these spatial patterns were statistically analyzed by creating a design of experiments with three levels in each variable and then identifying surface response models from the experimental data; more details of this study can be found in the Appendix A. Subsequent analysis of thermodynamic degrees of freedom for a system consisting of both oxides, Cu_2O and CuO, revealed that these patterns are due to the coexistence of both copper oxides at a unique critical oxygen partial pressure for a given temperature. To complete this study, a one-dimensional oxygen transport model was

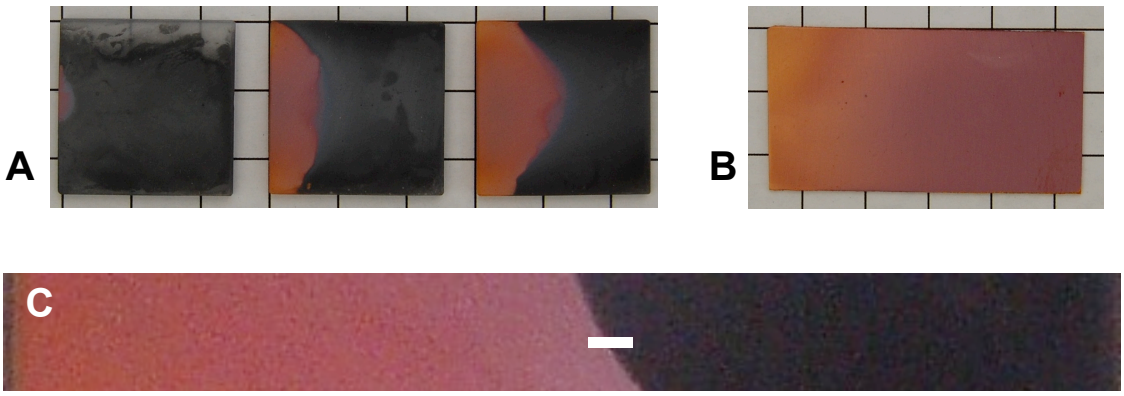

Figure 1.1: *Deposited films of Cu_2O and CuO on two different types of substrates. Figure A shows Cu_2O (red color) and CuO (black color) deposited on a 1 inch by 1 inch quartz substrate, where oxygen flow rate is reduced from left to right. Figure B shows Cu_2O deposited on a copper substrate. Figure C shows a close up to the sharp transition from Cu_2O to CuO on the quartz substrates. The length of the white line is 1 mm.*

created to estimate the location of the sharp Cu_2O-CuO transition on the films. The model was able to predict qualitatively the influence of the temperature and oxygen composition on the spatial patterns observed during the design of experiments.

The next step in modeling this deposition system was to include a deposition mechanism for copper and oxygen on the substrates in combination with the species transport equations. This not only increased the overall complexity of the deposition model, but introduced the additional requirement of computing kinetic constants unavailable in the literature. Furthermore, while operation of this CVD reactor may appear to be at steady state, the film is growing under non-equilibrium conditions. Therefore the need to simulate this system with at least two different time scales combined with the lack of a some kinetic information motivated the creation of the methodology presented in this thesis.

1.1.2 Modeling chemical vapor deposition (CVD)

Chemical vapor deposition (CVD) processes are widely used in the semiconductor manufacturing industry. In this process, a gaseous mixture of precursor species containing the desired materials for the film flows over a substrate where the precursors deposit and react with the surface to form a thin film.

A detailed kinetic mechanism is vital in modeling the complex chemical reaction system of CVD processes for design, optimization and control. However, a detailed kinetic model involves a large number of kinetic parameters to be determined, either from literature or experimentally. Furthermore, the scales of the kinetic parameters can inherently differ from each other over several orders of magnitude making the model stiff and computationally demanding.

The computational cost increases with the number of precursor species, creating a high-dimensional system, especially when gas phase and surface transport phenomena are coupled to the gas and surface reacting rate expressions. It is therefore advantageous to develop a framework to reduce the order of these chemical reaction systems models, while enabling the tracking of the evolution of the composition of species along the reactor in a time scale that allows sufficient accuracy for prediction and control.

In this thesis, a systematic model reduction methodology that is independent of the form of the reaction rate models is proposed. The methodology is based on a reaction Gauss-Jordan factorization procedure that allows a recasting of the modeling equations into a singular perturbation problem. The methodology is tested

first with simple deposition models and then is applied to the copper chemical vapor deposition processes.

1.2 Model reduction and stiffness relaxation background

Some of the first researchers to describe a methodology for reducing models of reaction systems were Mass and Pope in [15] and Lam and Goussis in [16]. The objective of Mass and Pope was to simplify complex chemical kinetics by reducing the dimensionality of the state space; Lam and Goussis aimed to decouple slow and fast time scales and overcome the stiffness of the differential equation system. While their goals in model reduction were different, they both used a similar approach based on the concept of dynamical systems.

On the one hand, Mass and Pope noted that when solving a complete model with detailed kinetics the trajectories in the composition state space tend to approach one another before equilibrium is reached creating an attracting manifold. From this observation they developed a perturbation analysis of the eigenvalues of the Jacobian of the system of differential equations to identify the trajectories for which certain eigenvectors vanished. These vanishing trajectories were associated with fast time scales that were then eliminated to reduce the model to only the variables that define a manifold. The reaction system then evolves on this manifold that roughly represents states that are in pseudo-equilibrium with respect to the fastest relaxing time scales.

On the other hand, Lam and Goussis used a computational singular pertur-

bation approach to find a refined a basis vector to separate the time scales. The basis vector is defined so that the vector product of the stoichiometric vector and the reaction rate vector is diagonal or block diagonal and thus can separate the time scales of the system. The method developed in [16] was later extended to application in reaction-diffusion systems in [17] to try to reduce stiffness due to reaction and diffusion processes. In the methodology proposed in this thesis, instead of an eigenvector analysis of the Jacobian of the system or refining a basis vector, the separation of times scales is carried out with a Gauss-Jordan factorization.

As seen in the works [15] and [16], the singular perturbation theory provides a natural framework for model reduction. In general if the system can be modeled in the standard singularly perturbed form, where the time scales are explicitly separated by a small parameter ϵ, then the system can be reduced to a system of differential-algebraic equations (DAE). However there is a wide range of systems that can exhibit time-scale multiplicity in which the slow and fast dynamics cannot be associated with specific process variables. In these cases it is necessary to use a coordinate change that would allow explicit separation of the time scales. Researchers Kumar, Christofides and Daoutidis proposed such a coordinate change to model chemical processes with two time scales in [18].

In their proposed methodology, Kumar et. al. define the algebraic variables as the limit of the physical constraints in the slow time scale at the limit $\epsilon \to 0$, and base the coordinate change on these algebraic variables and the Lie derivative of the physical constraints. Furthermore, they provide necessary and sufficient conditions for the existence of a ϵ-dependent and of an ϵ-independent coordinate change based

on the involutivity[1] of the matrix that weights the algebraic variables.

Vora and Dautidis [19] provided further insight into the construction of the coordinate changes for nonlinear systems. To do this they defined a generalized stoichiometric matrix that contained the stoichiometric coefficients of the chemical reactions in the system and separate this matrix into two matrices containing the columns for fast and slow reactions, respectively. Then they enforced linear independence on the matrix with the stoichiometric coefficients of the fast reactions as well as on the vector containing the reaction rates for the fast reactions. Consequently they noted that the involutivity condition of the distribution spanned by the columns of the stoichiometric matrices for the fast reactions is readily satisfied for isothermal systems since the matrix does not contain state variables. Therefore the new coordinates were a linear combination of the original coordinates where the transformation coefficients belong to the null space of the transpose of the matrix with the fast reactions stoichiometric coefficients. They also noted that the algebraic equations in the DAE representation of the problem obtained after the coordinate transformation corresponded to reaction equilibrium or complete conversion constraints.

Contou-Carrere and Daoutidis developed a model reduction method for reaction-convection processes with the goal of eliminating the stiffness from the systems in [20]. They used a combination of the method of characteristics and singular perturbation theory because modal decomposition techniques cannot be applied to

[1]Involutivity is the property of a matrix to be its own inverse. e.g $A^2 = I$ where I is the identity matrix

reaction-*convection* systems since all the eigenmodes of the spatial differential operator in these systems have the same amount of energy. After applying the method of characteristics, they use singular perturbation theory to separate spatial from temporal variables.

In the methodology presented in this thesis the coordinate change is provided through the reaction factorization. This factorization, although simple in nature, provides a coordinate transformation matrix that identifies conserved quantities directly. Likewise, the approach developed in this thesis provides a rigorous means of separating modeling time scales, resulting in a "nested" sequence of singular perturbation problems for transient deposition models that are spatially dependent. These and additional benefits and features of the reaction factorization method will be described in the following chapters of this thesis.

Chapter 2

Methodology

This chapters describes the reaction factorization methodology for a lumped deposition model. The ability of the factorization to guide the separation of times scales is explored through a simplified deposition reaction system and a procedure to solve the singular perturbation problem resulting from the reaction factorization is outlined.

2.1 Reaction factorization on a lumped model deposition system

To illustrate the methodology proposed in this thesis, consider a simplified deposition mechanism consisting of a gas-phase monomer M and a gas phase trimer T species and the reversible reaction between the two[1]. A molecule of precursor monomer M, deposits a single atom of material A through an irreversible reaction with a surface site X producing the growth of the film, as sketched in Figure 2.1 where the net-forward reversible and deposition reaction rates are represented by G_0 and F_0, respectively. In this analysis it is assumed that the net-forward rate associated with the reversible reaction is much greater than the rate of the deposition reaction. Secondary products of the surface reaction are not considered in this

[1]While the choice of a trimer species may seem at first unusual relative to a dimer, we will show later that Cu_3I_3 is the only oligomer formed in the gas phase from CuI

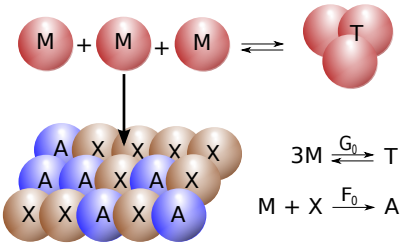

$$G_0 = \frac{1}{\epsilon}\left(K_0\,[\mathrm{M}]^3 - [\mathrm{T}]\right) \qquad \mathrm{mol\ m^{-3}\ s^{-1}}$$

$$F_0 = k_0\,[\mathrm{M}]\,[\mathrm{X}] \qquad \mathrm{mol\ m^{-2}\ s^{-1}}$$

Figure 2.1: *Schematic of the simplified deposition mechanism. Monomer precursor M reversibly produces the trimer T in the gas phase, and can be deposited through an irreversible reaction with a surface site X to produce an adsorbed species A in the film.*

simplified analysis. Material balances for each species yield the following ordinary differential equations in time:

$$\frac{d\mathbf{c}^{n_c\times 1}}{dt} = \mathbf{S}^{n_c\times n_r}\mathbf{r}^{n_r\times 1} \quad \Longrightarrow \quad \frac{d}{dt}\begin{bmatrix}[M]\\ [T]\\ \sigma\,[X]\\ \sigma\,[A]\end{bmatrix} = \begin{bmatrix}-3 & -1\\ 1 & 0\\ 0 & -1\\ 0 & 1\end{bmatrix}\begin{bmatrix}G_0\\ \sigma F_0\end{bmatrix} \tag{2.1}$$

where σ is the deposition surface area to reactant gas volume ratio with units m^{-1}. The matrices $\mathbf{c}$, $\mathbf{S}$, and $\mathbf{r}$ contain the species concentrations, stoichiometric coefficients, and reaction rates respectively. n_c and n_r refer to the number of chemical species and reactions. The species concentrations are given in $\mathrm{mol/m^3}$ for gas phase, [M] and [T], and $\mathrm{mol/m^2}$ for [X] and [A].

This original formulation (2.1) of the problem presents a higher-dimensional set of ODEs, four equations, compared to the single rate-limiting deposition step. Moreover, the dynamic behavior of the monomer concentration, $[\mathrm{M}]\,(t)$ is governed by two reaction rates of different orders of magnitude.

It might initially appear that the QR or singular value decomposition methods

would be the best candidates to diagonalize the system of differential equations 2.1 and to subsequently reduce it to its minimal dynamic dimension. Nevertheless, these methods are not useful for guiding the separation of time scales because the matrix $\mathbf{S}$ is defined by reaction stoichiometric coefficients instead of reaction rate coefficients. On the other hand, a Gauss-Jordan factorization of $\mathbf{S}$ can provide guidance in the time scale separation by pairing each reaction with each new reaction coordinate to the greatest extent possible, similar to the approach of Vora and Daoutidies in [19]. Hence, dynamic dimension reduction and time scale separation in Equation 2.1 can be obtained if a transformation matrix $\mathbf{U}$ exists such that in the coordinate change $\mathbf{y} = \mathbf{U}\mathbf{c}$ each new coordinate can be associated to each reaction rate, $y_i \in \mathcal{R}^{n_c}$, i.e.,

$$\mathbf{U}^{n_c \times n_c}\mathbf{S}^{n_c \times n_r} \approx \begin{bmatrix} \mathbf{I}^{n_r \times n_r} \\ \mathbf{0}^{(n_c - n_r) \times n_r} \end{bmatrix}.$$

Clearly, complete diagonalization of the stoichiometric matrix should not be expected in every case. However, this factorization can still guide the time scale separation even if off-diagonal elements remain. For the system under study in this section, the ODEs in Equation 2.1 can be factored to find

$$\frac{d\mathbf{y}}{dt} = \frac{d}{dt}\begin{bmatrix} [T] \\ -[M] - 3[T] \\ \sigma[X] - [M] - 3[T] \\ \sigma[A] + [M] + 3[T] \end{bmatrix} = \frac{d}{dt}\begin{bmatrix} z_0 \\ x_0 \\ w_0 \\ w_1 \end{bmatrix} = \begin{bmatrix} 1 & 0 \\ 0 & 1 \\ 0 & 0 \\ 0 & 0 \end{bmatrix}\begin{bmatrix} G_0 \\ \sigma F_0 \end{bmatrix} \tag{2.2}$$

yielding the following temporal modes for the specific case $k_0 = 1$ $\mathrm{m^3 mol^{-1} s^{-1}}$,

$K_0 = 1\ \mathrm{m^3 mol^{-1}}$, and $\sigma = 1\ \mathrm{m^{-1}}$:

$$\text{fast (reversible)} \qquad \frac{dz_0}{dt} = \frac{d[T]}{dt} = \frac{1}{\epsilon}\left([M]^3 - [T]\right) \tag{2.3}$$

$$\text{slow (deposition)} \qquad \frac{dx_0}{dt} = \frac{d(-[M] - 3[T])}{dt} = [M][X] \tag{2.4}$$

$$\text{conserved quantities} \qquad w_0 = [X] - [M] - 3[T] \tag{2.5}$$

$$w_1 = [A] + [M] + 3[T] \tag{2.6}$$

or more generally, when the factorization 2.2 can be completed,

$$\text{slow} \qquad \frac{d\mathbf{x}}{dt} = \frac{d\mathbf{U}_x\mathbf{c}}{dt} = \mathbf{F}(\mathbf{c}) \qquad\qquad \frac{d\mathbf{x}}{dt} = \mathbf{F}(\mathbf{x}, \mathbf{z}, \mathbf{w}_o) \tag{2.7}$$

$$\text{fast} \qquad \frac{d\mathbf{z}}{dt} = \frac{d\mathbf{U}_z\mathbf{c}}{dt} = \frac{1}{\epsilon}\mathbf{g}(\mathbf{c}) \qquad \stackrel{\epsilon\to 0}{\Longrightarrow} \qquad 0 = \mathbf{g}(\mathbf{x}, \mathbf{z}, \mathbf{w}_o) \tag{2.8}$$

$$\text{conservation} \qquad \mathbf{w} = \mathbf{U}_w\mathbf{c} \tag{2.9}$$

where $\mathbf{G} = \mathbf{g}/\epsilon$. We observe a *semi-explicit* differential-algebraic (DAE) system results, both in the form of example (2.3-2.6) and in the more general case (2.7-2.9); algebraic equations result from both the elimination of reduntant dynamic modes producing the conserved quantities, and as will be discussed later, as $\epsilon \to 0$.

Following the nomenclature by Biegler in [21], $\mathbf{x}$ are the differential variables, $\mathbf{z}$ the algebraic variables, and $\mathbf{y}^T = [\mathbf{x}^T\, \mathbf{z}^T\, \mathbf{w}^T]$ [21]. $\mathbf{U}_x, \mathbf{U}_z, \mathbf{U}_w$ are submatrices from $\mathbf{U}$ containing the rows corresponding to the slow, fast and conservation new coordinates, $\mathbf{x}, \mathbf{y}, \mathbf{z}$, respectively. It should be observed that new coordinates $\mathbf{w}$ reveal quantities conserved during the time evolution the slow modes. For example,

w_1 is simply the total number of deposition element atoms in our control volume and $w_0 + w_1 = [X] + [A]$ corresponds to the conservation of surface states. It is important to recall that the decomposition approach presented here resembles other model reduction procedures such as the ones in [18, 19, 22, 23] with the differences noted in the introduction section of the thesis.

2.1.1 Integration of the DAE system in time

The system of differential-algebraic equations resulting from the reaction factorization in equations 2.4-2.6 can be integrated in a relatively direct manner for a finite ϵ. The ODEs involving $\mathbf{x}$ and $\mathbf{z}$ are integrated in time by computing the reaction rates in the original coordinates by first recovering $\mathbf{c}$ with the inverse of the transformation matrix from $\mathbf{c} = \mathbf{U}^{-1}\mathbf{y}$. It is evident that $\mathbf{U}$ must be invertible since the forward elimination procedure used to obtain it is reversible. It should also be noted that the new coordinates representing the conserved quantities $\mathbf{w} = \mathbf{w}_o$ are clearly constant for all time.

Figure 2.2 shows representative results for the DAE system in equations 2.4-2.6 calculated using a fixed step-size implicit Euler integrator. The initial specified conditions used are $\mathbf{c}_o = [0.4, 0.6, 1, 0]^T$ resulting in $x_o = -2.2$, $z_o = 0.6$, and $\mathbf{w}_o = [-1.2, 2.2]^T$ after the transformation. The figure illustrates the strong attraction of the initial conditions $\mathbf{c}_o$ to the neighborhood of the equilibrium manifold $\mathcal{Q}$ and the subsequently slower dynamics which follow. The nature and computation of manifold $\mathcal{Q}$ are described next.

2.1.2 Outer solution of the singular perturbation problem

The reaction system takes the form of a singularly perturbed ordinary differential equation when Equation 2.3 is multiplied by ϵ. Furthermore, in the limit $\epsilon \to 0$ the fast dynamics in the species composition space vanish, relaxing the system to the manifold defined by the equilibrium condition

$$\mathcal{Q} = \left\{ \; [M], [T] \; : \; K_0[M]^3 - [T] = 0 \right\}. \tag{2.10}$$

The numerical outer solution of the singular perturbation problem [24] with initial conditions $\mathbf{c}_o$ is calculated in the following manner.

First, the initial specified conditions $\mathbf{c}_o = \mathbf{c}(t = 0)$ are converted to the new chemical species composition space using the transformation matrix $\mathbf{U}$, i.e $\mathbf{y}_o = \mathbf{U}\mathbf{c}_o$. Then these initial conditions $\mathbf{c}_o$ are projected onto the equilibrium manifold $\mathcal{Q}$ defined by (2.10), to find $\mathbf{c}^0$ by solving the set of nonlinear/linear algebraic equations:

$$\begin{bmatrix} \mathbf{U}_x\mathbf{c}^0 \\ \mathbf{g}(\mathbf{c}^0) \\ \mathbf{U}_w\mathbf{c}^0 \end{bmatrix} = \begin{bmatrix} \mathbf{x}_o \\ \mathbf{0} \\ \mathbf{w}_o \end{bmatrix}.$$

It is important to notice that while the manifold $\mathcal{Q}$ is defined in the original coordinates, i.e. $[M]$ and $[T]$, the above set of nonlinear/linear equations gives the initial conditions in the new coordinate space $\mathbf{y}$. The current state of the new coordinates for the species state $\mathbf{c}^i$ at time t^i (where $i = 0$ for the projected initial state) is then computed during the integration process using the transformation matrix $\mathbf{U}_x$.

$$\mathbf{x}^i = \mathbf{U}_x\mathbf{c}^i.$$

Finally we use a Newton-Raphson or another suitable nonlinear algebraic equation solver to calculate the implicit Euler update over time step Δ_t by solving driving the residual below to zero.

$$\begin{bmatrix} (\mathbf{x}^{i+1} - \mathbf{x}^i)/\Delta_t - \mathbf{f}\left(\mathbf{U}^{-1}\mathbf{y}^{i+1}\right) \\ \mathbf{g}\left(\mathbf{U}^{-1}\mathbf{y}^{i+1}\right) \\ \mathbf{w}^{i+1} - \mathbf{w}_o \end{bmatrix}.$$

Figure 2.2 shows the results of applying this method to the system in equations 2.3-2.6 for $\epsilon = 0$. The figure shows the specified initial conditions $\mathbf{c}_o$, the projection of these conditions into the equilibrium manifold $\mathcal{Q}$ to give the initial conditions $\mathbf{c}^0$, and the evolution in time of the system along the manifold approaching equilibrium at the point $\mathbf{c}_\infty$.

2.1.3 DAE index

It should be mentioned that when solving semi-explicit DAE systems one must be concerned about the index of the system and the consistency of initial conditions. The index of a DAE is defined as the number of times that the system must be differentiated with respect to time in order to convert it into an explicit set of first order ODEs [25]. For DAE systems with index higher than one, the differentiation to reduce the index to one generates more algebraic variables. Consistent initial values are those who satisfy not only the original algebraic variables but also the ones resulting from the index reduction [26].

The semi explicit DAE system in equations 2.3-2.6 is index-1, thus consistency of the initial conditions is not an issue in this case. Nonetheless, more complex

deposition surface reaction models may have higher DAE index values and thus need more sophisticated treatment of the initial conditions [21, 27].

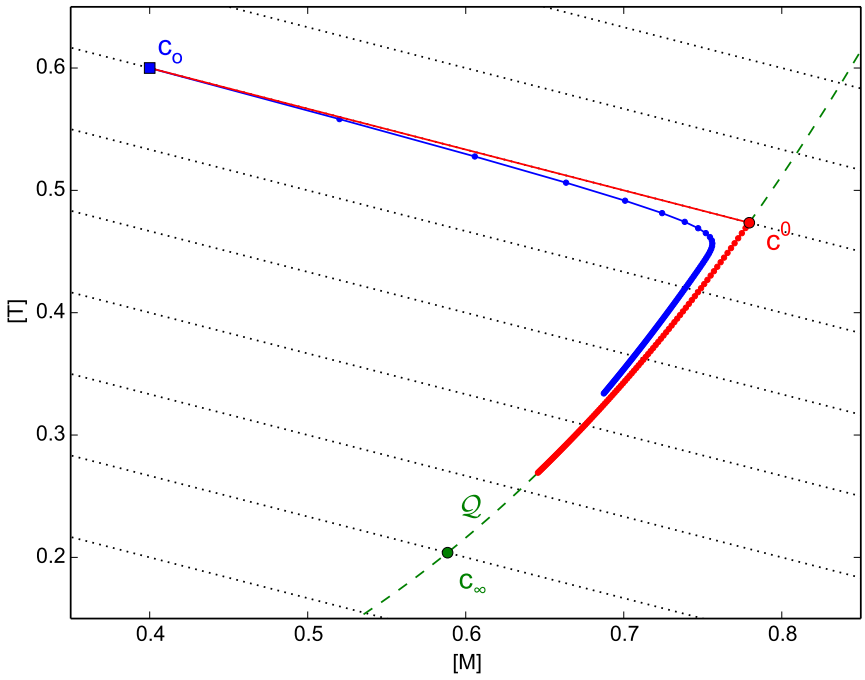

Figure 2.2: Two-dimensional dynamics with $k_0 = K_0 = 1$, $\sigma = 1$, and $t \in [0, 2]$. Specified initial conditions and those projected onto the equilibrium manifold (green dashed curve $\mathcal{Q}$) are marked with the filled blue square and red circle, respectively. Each point denotes 0.02 time units; black dotted lines denote $[M] + 3[T] = \mathit{constant}$. The blue curve corresponds to $\epsilon = 0.1$ and the wto ODE model; the red trajectory represents the outer solution of the singular perturbation problem.

2.1.4 High net-forward rates and multiple deposition reactions

Another numerical challenge encountered when solving models of surface reactions arises when the equilibrium reactions favor the product species and the deposition reaction rate is significant. Under these conditions the numerical implicit

integrator may converge to negative values of reactant concentrations and provide results with non-physical meaning. To illustrate this consider the following reaction system

$$\mathrm{M} + 2\mathrm{N} \overset{G_0}{\rightleftharpoons} \mathrm{P}$$

$$\mathrm{D} + \mathrm{E} \overset{F_0}{\rightarrow} \mathrm{B}$$

with the net-forward reaction rates

$$\frac{d[M]}{dt} = -G_0$$

$$\frac{d[N]}{dt} = F_0 - G_0$$

$$\frac{d[P]}{dt} = G_0$$

where the reactants D and E are fed in such a way that the rate F_0 is constant. The matrix representation of the system is given by

$$\frac{d}{dt}\begin{bmatrix} [P] \\ [N] \\ [M] \end{bmatrix} = \begin{bmatrix} 1 & 0 \\ -2 & 1 \\ -1 & 0 \end{bmatrix} \begin{bmatrix} G_0 \\ F_0 \end{bmatrix}$$

with $G_0 = \frac{1}{\epsilon} g_0$; after applying the factorization the system becomes

$[M] + [P] = w_0$ the conserved mode

$[N] + [P] = x_0 + \Delta_t F_0$ the slow mode evolving over time interval Δ_t

then the equilibrium manifold is defined by g_0=0 and the integration of the slow mode to give the equations:

$$[P] - K_0[M][N] = 0$$

$$x_0 + \Delta_t F_0 - [N] - K_0\left(w_0 - x_0 - \Delta_t F_0 + [N]\right)[N] = 0$$

Setting the equilibrium constant $K_0 = 1$ and solving for $[N]$ results in

$$[N] = \frac{x_0 + \Delta_t F_0 - 1 - w_0 \pm \sqrt{(1 + w_0 - x_0 - \Delta_t F_0)^2 + 4(x_0 + \Delta_t F_0)}}{2}$$

thus, even though only the positive solution for $[N]$ has a physical meaning, if $K_0 \gg 1$ the numerical integrator can overshoot the limit $[M] \to 0$ and converge to the negative solution as mentioned above.

Finally, the presence of multiple, relatively slow deposition reactions that all deposit the same chemical species may prevent the reaction factorization from fully diagonalizing the stoichiometric matrix. However, as mentioned before, the result may still be valid and useful for guiding the dimension reduction and separation of time scales. For example consider adding the following deposition reaction to the system of equations 2.1.

$$T + X \quad \xrightarrow{F_1} \quad A + 2M \qquad\qquad F_1 = k_1[T][X] \tag{2.11}$$

using the same values for the reversible and deposition reaction constants as in the analysis above, $k_0 = K_0 = 1$, and $k_1 = 0$ the resulting DAE is

$$\begin{aligned}
\text{slow} \quad & \frac{dx_0}{dt} = \frac{d([M] + 3[T])}{dt} = -[M][X] - [T][X] \\
\text{fast} \quad & \frac{dz_0}{dt} = \frac{d[T]}{dt} = \frac{1}{\epsilon}\left([M]^3 - [T]\right) - [T][X] \quad \xrightarrow{\epsilon \to 0} \quad [M]^3 - [T] = 0 \\
\text{conserved} \quad & w_0 = [X] + [A] \\
& w_1 = [A] + [M] + 3[T].
\end{aligned}$$

In this case it can be seen that the conserved quantities are the same as those obtained before the addition of the new deposition reaction (2.11): the conservation of

surface states and the conservation of the deposited material found in species M, T, and A. The equilibrium relationship resulting is also the same, and a single dynamic mode now describes the consumption of the total precursor by the combination of both surface reactions. The kinetic model considered for copper CVD in Chapter 4 presents this case where the factorization does not fully diagonalize the system. However, the model is structurally correct and the singular perturbation problem will be shown to be valid.

Chapter 3

Reaction factorization on a spatially distributed deposition system

This chapter studies the reaction factorization of a spatially distributed deposition system, extending the analysis in the previous chapter by considering gas phase species diffusion in the hot wall tubular reactor. This model provides a more realistic CVD process relative to the lumped parameter model in Chapter 2, and is more closely related to our copper deposition system.

3.1 Simplified deposition system

To demonstrate the next step in extending the reaction factorization procedure, consider a model CVD system in which (metal) precursor monomer species M in the gas phase adsorbs onto the growth surface to form the adsorbed species A with net adsorption rate G_1; monomer M also can undergo a trimerization reaction to form T at a rate G_0. The adsorbed species is incorporated into the growing film B through an irreversible reaction at rate F_0; this same rate governs the time-evolution of a film property L, such as film thickness, by the rate δF_0, where δ relates

the concentration of deposited species B to the film property.

$$
\begin{aligned}
3M &\Leftrightarrow T \qquad G_0 = \frac{1}{\epsilon_0}\left(K_0\,[\mathrm{M}]^3 - [\mathrm{T}]\right) \qquad \text{mol s}^{-1}\text{m}^{-3} \\
M &\Leftrightarrow A \qquad G_1 = \frac{1}{\epsilon_1}\left(K_1\,[\mathrm{M}] - [\mathrm{A}]\right) \qquad \text{mol s}^{-1}\text{m}^{-2} \\
A &\rightarrow B \qquad F_0 = k_0\,[\mathrm{A}] \qquad \text{mol s}^{-1}\text{m}^{-2}
\end{aligned}
\tag{3.1}
$$

The reactions and their associated rate expressions are summarized in Equation 3.1, where K_0 is the equilibrium constant associated with the trimerization reaction with units $\text{mol}^{-2}\text{m}^6$, K_1 is adsorption equilibrium coefficient with units of m, and k_0 is the forward rate constant of the irreversible reaction with units of s^{-1}.

The small parameters $\epsilon_i \ll 1$ represent the time-scale ratios (with units of s) of the reversible reactions relative to the irreversible reaction, which is assumed to be the rate-limiting step of this example. These small parameters mark the separation of fast and slow modes in the singular perturbation formulation of the problem; a physical interpretation of this system is that the deposition process is kinetically limited.

3.1.1 Tubular deposition reactor model

The deposition reactions will take place in a tubular reactor system, as the one depicted in Figure 3.1, and thus a heterogeneous plug flow reactor (PFR) model with axial diffusion and convection of the gas-phase precursors is derived; the axial coordinate is denoted ζ. For this reactor system, the start of the deposition zone is $\zeta = 0$ and, without loss of generality, we set the reactor outlet as $\zeta = 1$ m. As in

the previous chapter, surface and gas-phase molar concentrations are indicted with the bracket notation $[\cdot]$.

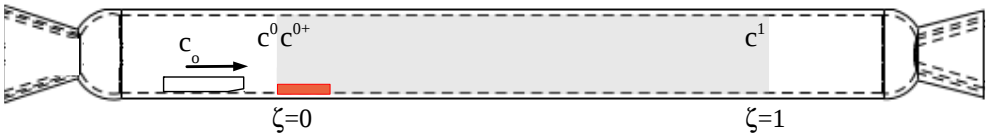

Figure 3.1: *Tubular reactor schematic. Precursor M evaporates from a precursor boat (white rectangle) and flows toward the deposition zone* $0 \leq \zeta \leq 1$. c_o *represents the specified boundary conditions in which we assume a constant concentration of M in the gas phase upstream from the deposition zone.* c^0 *is the projection of the specified boundary conditions onto the manifold* $\mathcal{Q}$ *(defined in (3.5).* c^{0^+} *and* c^1 *are the concentrations resulting from boundary conditions at* ζ_0 *and at* ζ_1*, respectively, in the two-point boundary value problem resulting from the factorization.*

The modeling equations are summarized in Table 3.1, where

$$J_i = -\mathcal{D}_i \frac{\partial [\mathrm{i}]}{\partial \zeta} + v\,[\mathrm{i}]$$

is the flux (diffusion and convection) of species i. Only binary diffusion is considered due to the low concentration of precursors. The parameter σ is the area-to-volume ratio to convert surface concentration into volume based concentrations. Thus, for a tubular reactor system of radius R where material is deposited on the inner wall surface, $\sigma = 2/R$. The small parameter $\delta \ll 1$ captures the ratio of the deposition time scale to the species transport time scale. Because of these small parameters, the rates of change in the surface states can differ in orders of magnitude, rendering the system numerically stiff.

Governing equation	$\zeta = 0,\ t \geq 0$	$\zeta = 1,\ t \geq 0$	$\zeta \in (0,1),\ t = 0$
$\dfrac{\partial [T]}{\partial t} = \dfrac{\partial J_T}{\partial \zeta} + G_0$	$J_T(0) = u\,[\mathrm{T}]_0$	$\dfrac{\partial\,[\mathrm{T}]}{\partial \zeta} = 0$	$[\mathrm{T}] = 0$
$\dfrac{\partial [M]}{\partial t} = \dfrac{\partial J_M}{\partial \zeta} - 3G_0 - \sigma G_1$	$J_M(0) = u\,[\mathrm{M}]_0$	$\dfrac{\partial\,[\mathrm{M}]}{\partial \zeta} = 0$	$[\mathrm{M}] = 0$
$\dfrac{\partial [A]}{\partial t} = G_1 - F_0$	$----$	$----$	$[\mathrm{A}] = 0$
$\dfrac{\partial \mathrm{L}}{\partial t} = F_1$	$----$	$----$	$\mathrm{L} = 0$
$\dfrac{\partial [B]}{\partial t} = F_0$	$----$	$----$	$[\mathrm{B}] = 0$

Table 3.1: *Modeling equations for the heterogeneous tubular CVD system together with boundary and initial conditions.*

3.1.2 Reaction factorization and the singular perturbation problem

To eliminate redundant dynamic modes and to provide a rational path to reconfiguring the modeling equations so that the system dynamics as $\epsilon_0, \epsilon_1, \delta \to 0$ can be investigated, the Gauss-Jordan factorization procedure proposed in Chapter 2 is applied to allow separating the effect of each reaction to guarantee the correct handling of the different time scales of the model. Rewriting the modeling equations in matrix form

$$\frac{\partial}{\partial t}\begin{bmatrix} [\mathrm{T}] \\ [\mathrm{M}] \\ [\mathrm{A}] \\ \mathrm{L} \\ [\mathrm{B}] \end{bmatrix} = \begin{bmatrix} \partial J_T/\partial\zeta \\ \partial J_M/\partial\zeta \\ 0 \\ 0 \\ 0 \end{bmatrix} + \begin{bmatrix} 1 & 0 & 0 & 0 \\ -3 & -\sigma & 0 & 0 \\ 0 & 1 & -1 & 0 \\ 0 & 0 & 0 & 1 \\ 0 & 0 & 1 & 0 \end{bmatrix} \begin{bmatrix} G_0 \\ G_1 \\ F_0 \\ F_1 \end{bmatrix}$$

or

$$\frac{\partial \mathbf{c}}{\partial t} = \frac{\partial \mathbf{J}}{\partial \zeta} + \mathbf{S} \begin{bmatrix} G_0 \\ G_1 \\ F_0 \\ F_1 \end{bmatrix}.$$

To find the transformation matrix $\mathbf{U}$ the factorization is applied to the stoichiometric matrix, $\mathbf{S}$, of the kinetic mechanism of our system yielding

$$\mathbf{S}_F = \mathbf{U}\cdot\mathbf{S} = \begin{bmatrix} 1 & 0 & 0 & 0 & 0 \\ 3 & 1 & 0 & 0 & 0 \\ 3 & 1 & \sigma & 0 & 0 \\ 0 & 0 & 0 & 1 & 0 \\ 3 & 1 & \sigma & 0 & \sigma \end{bmatrix} \cdot \begin{bmatrix} 1 & 0 & 0 & 0 \\ -3 & -\sigma & 0 & 0 \\ 0 & 1 & -1 & 0 \\ 0 & 0 & 0 & 1 \\ 0 & 0 & 1 & 0 \end{bmatrix} = \begin{bmatrix} 1 & 0 & 0 & 0 \\ 0 & -\sigma & 0 & 0 \\ 0 & 0 & \sigma & 0 \\ 0 & 0 & 0 & 1 \\ 0 & 0 & 0 & 0 \end{bmatrix}. \tag{3.2}$$

Multiplying the original state vector by the transformation matrix yields a set of new coordinates given by

$$\mathbf{y} = \mathbf{U}\cdot\mathbf{c} = \begin{bmatrix} 1 & 0 & 0 & 0 & 0 \\ 3 & 1 & 0 & 0 & 0 \\ 3 & 1 & \sigma & 0 & 0 \\ 0 & 0 & 0 & 1 & 0 \\ 3 & 1 & \sigma & 0 & \sigma \end{bmatrix} \cdot \begin{bmatrix} [\mathrm{T}] \\ [\mathrm{M}] \\ [\mathrm{A}] \\ \mathrm{L} \\ [\mathrm{B}] \end{bmatrix} = \begin{bmatrix} [\mathrm{T}] \\ 3[\mathrm{T}] + [\mathrm{M}] \\ 3[\mathrm{T}] + [\mathrm{M}] + \sigma[\mathrm{A}] \\ \mathrm{L} \\ 3[\mathrm{T}] + [\mathrm{M}] + \sigma[\mathrm{A}] + \sigma[\mathrm{B}] \end{bmatrix} = \begin{bmatrix} z_0 \\ z_1 \\ x_0 \\ x_1 \\ w_0 \end{bmatrix} \tag{3.3}$$

After applying the factorization to the boundary and initial conditions, our model transforms into the set of equations shown in Table 3.2. The table shows that the model of the system in the new coordinates $\mathbf{y}$, which are the linear combinations of the original coordinates given in Equation 3.3. Note that the model equations for each of the new coordinates involve only one net forward reaction rate, which allows us to separate unambiguously the different time scale modes of the system.

The fast modes (for $0 < \epsilon_i \ll 1$) are tracked by the new coordinates z_0 and z_1, which are the concentration of monomer and the total concentration of precursor on the gas phase, respectively. Multiplying both equations by their respective small parameter, ϵ_0 and ϵ_1, and taking the limits as the parameters go to zero, the outer

Governing equation	$\zeta = 0,\ t \geq 0$	$\zeta = 1,\ t \geq 0$	$t = 0,\ 0 < \zeta < 1$
$\dfrac{\partial z_0}{\partial t} = \dfrac{\partial J_T}{\partial \zeta} + G_0$	$J_{z_0}(0) = z_0 u$	$\dfrac{\partial z_0}{\partial \zeta} = 0$	$z_0 = 0$
$\dfrac{\partial z_1}{\partial t} = \dfrac{\partial \left(3J_T + J_M\right)}{\partial \zeta} - \sigma G_1$	$J_{z_1}(0) = u z_1$	$\dfrac{\partial z_1}{\partial \zeta} = 0$	$z_1 = 0$
$\dfrac{\partial x_0}{\partial t} = \dfrac{\partial \left(3J_T + J_M\right)}{\partial \zeta} - \sigma F_0$	$J_{x_0}(0) = u x_0$	$\dfrac{\partial x_0}{\partial \zeta} = 0$	$x_0 = 0$
$\dfrac{\partial x_1}{\partial t} = F_1$	$----$	$----$	$\mathrm{L} = 0$
$\dfrac{\partial \left(w_0 - \delta x_1\right)}{\partial t} = 0$	$----$	$----$	$\mathrm{L} = \text{constant} + \delta\,[\mathrm{B}]$

Table 3.2: *Model structure after factorization.*

solutions of the first two singularly perturbed PDEs are found by

$$g_0 = 0 \quad \text{and} \quad g_1 = 0$$

where $G_i = g_i/\epsilon_i$.

The new coordinate w_0 is a conservation mode, because the corresponding row of the transformed stoichiometric matrix $\mathbf{S}_F$ of Equation 3.2 vanishes, meaning it has no generation or consumption terms. Furthermore, combining the variables x_1 and w_0 yields a conservation mode given by the fifth equation in Table 3.2, that indicates that the final conserved quantity gives

$$L = \text{constant} + \delta[B] = \mathbf{w}_o + \delta[B]$$

which means the constant is w_0 and represents the initial thickness or surface property value.

The slow modes of the system, variables x_0 and x_1, correspond to the total amount of precursor that has not been incorporated to the bulk of the film and to the thickness of the film, respectively. The system evolves along these slow modes during the slow time [28, 20]. Therefore defining the slow time $\tau = \delta t$, taking $F_1 = \delta F_0$ and recalling that $x_1 = \mathrm{L}$, we have that

$$\begin{aligned} \delta\frac{\partial x_0}{\partial \tau} &= \frac{\partial}{\partial \zeta}\left(3J_T + J_M\right) - \sigma F_0 \\ \frac{\partial \mathrm{L}}{\partial \tau} &= F_0 \end{aligned}$$

therefore, when $\delta \to 0$

$$\begin{aligned} 0 &= \frac{\partial}{\partial \zeta}\left(3J_T + J_M\right) - \sigma F_0 \\ \frac{\partial \mathrm{L}}{\partial \tau} &= F_0 \end{aligned}$$

In summary the evolution of the system in the slow time scale, along the manifold defined by the equilibrium relations g_0 and g_1, when $\epsilon_i \to 0$ and $\delta \to 0$, can be tracked by the following equations

$$g_0 = 0 \tag{3.4a}$$

$$g_1 = 0 \tag{3.4b}$$

$$\frac{d}{d\zeta}\left(3J_T + J_M\right) = \sigma F_0 \tag{3.4c}$$

$$\frac{dL}{d\tau} = F_0 \tag{3.4d}$$

Our system is now described by a mixture of differential and algebraic equations, a DAE system, plus boundary and initial conditions to be described next. To solve this system it is necessary to provide initial and boundary conditions that are consistent not only with the algebraic equations, but also with the differential equation 3.4c, in a manner referred to as consistent initialization [29].

The initial condition is defined as an empty reactor before the start of the deposition, shown in Equation 3.6, which fulfills trivially the equilibrium manifold given by

$$\mathcal{Q} = \{\mathbf{c} : g_0 = 0 \text{ and } g_1 = 0\} \tag{3.5}$$

in the gas phase

$$\begin{aligned} &[\mathrm{M}](\zeta, 0) = 0 \\ &[\mathrm{D}](\zeta, 0) = 0 \\ &[\mathrm{A}](\zeta, 0) = 0 \\ &\mathrm{L}(\zeta, 0) = 0 \end{aligned} \qquad 0 < \zeta < 1. \tag{3.6}$$

The specified boundary condition is $\mathbf{c}_o = [M_0, 0, 0]$, in which we assume a constant gas phase concentration of monomer on the boat zone as shown in Figure 3.1; furthermore Equation 3.2 is used to obtain the specified conditions in the new coordinate system. To translate these conditions to the slow time scale we project them onto the manifold $\mathcal{Q}$, this is the point $\mathbf{c}^0$ in Figure 3.1. Subsequently, $\mathbf{c}^0$ is used to define the boundary conditions for Equation 3.4c, assuming that the gas is moving at a uniform speed u. Since the system is constrained to the manifold $\mathcal{Q}$, equations 3.4a and 3.4b must be fulfilled together with the boundary conditions at $\zeta = 0$; this point is identified as $\mathbf{c}^{0^+}$ in Figure 3.1. The process for obtaining these boundary conditions is summarized in Table 3.3 and a phase space representation is given in Figure 3.4.

3.1.3 Representative results

As a representative simulation, consider an initially empty reactor with a $M_0 = 2$ $\mathrm{s}^{-1}\mathrm{m}^{-3}$mol feed of pure monomer. Kinetic parameters for Equation 3.1 and transport parameters used in this simulation are given in Table 3.4.

To solve our model described by Equation 3.4, one only needs to obtain the steady state spatial profiles of precursors and adsorbed species in the reactor using equations 3.4a through 3.4c, and then use this profile to integrate in time our tracked property L over the slow time scale τ using Equation 3.4d. As mentioned in the previous section, the first step in the solution of our model is to project the specified boundary condition, $\mathbf{c}_o$, onto the spatial distributions manifold to which the system

$\mathbf{c}_o$	$\mathbf{c}^0$	$\mathbf{c}^{0^+}$	$\mathbf{c}^1$
	Variables		
$[\mathrm{M}]_o = M_0$	$[\mathrm{M}]^0$	$[\mathrm{M}]^{0^+}$	$[\mathrm{M}]^1$
$[\mathrm{T}]_o = 0$	$[\mathrm{T}]^0$	$[\mathrm{T}]^{0^+}$	$[\mathrm{T}]^1$
$[\mathrm{A}]_o = 0$	$[\mathrm{A}]^0$	$[\mathrm{A}]^{0^+}$	$[\mathrm{A}]^1$
$x_{0_o} = M_0$	x_0^0	$x_0^{0^+}$	x_0^1
	Equations		
	$G_0 = 0$	$G_0 = 0$	$G_0 = 0$
	$G_1 = 0$	$G_1 = 0$	$G_1 = 0$
	$x_0 = \mathit{constant}$	$v{x_0}^0 = J_{x_0}(0^+)$	$\dfrac{\partial}{\partial \zeta}(x_0) = 0$

Table 3.3: *Boundary conditions as they are transformed from the specified conditions* $\mathbf{c}_o$ *to the projection onto the manifold* $\mathcal{Q}$, $\mathbf{c}^0$, *and finally to the boundary conditions at the start* (ζ_0) *and end* (ζ_1) *of the deposition zone,* $\mathbf{c}^{0^+}$ *and* $\mathbf{c}^1$, *respectively.*

is constrained by the equilibrium relationships g_0 and g_1 and the transport equation 3.4c in Equation 3.1 when $\epsilon_0, \epsilon_1, \delta \to 0$. Then these projected conditions are used to calculate the boundary condition at the beginning of the deposition zone; these conditions are shown in Figure 3.4.

The second step in the solution of our system is the solution of the two-point boundary value problem given by Equation 3.4c, the spatial differential equation that drives transport in the reactor, while making sure the equilibrium relationships in equations 3.4a and 3.4b hold for every integration point to ensure that the system stays on the manifold of spatial distributions $\mathcal{Q}$. For this, a set of collocation points,

Parameter	Value	Units
v	0.03	m/s
K_0	1	m^3mol^{-1}
K_1	1.5	m
k_0	0.4	s^{-1}
σ	1	m^2m^{-3}
$\mathcal{D}_M$	1.0×10^{-1}	m^2s^{-1}
$\mathcal{D}_D$	1.0×10^{-2}	m^2s^{-1}

Table 3.4: *Kinetic and transport parameters for representative simulation of equations 3.4*

ζ_i with $i = 0, 1, ..., N$, is defined in Figure 3.2 where $\zeta_0 = 0$ and $\zeta_N = 1$. We then com-

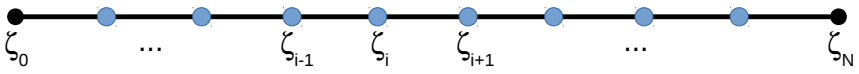

Figure 3.2: *Schematic of the collocation points in the ζ dimension.*

pute discretization arrays $\mathbf{E}$ and $\mathbf{F}$ using second order accurate finite differences to calculate the discretization weights of the second and first derivatives, respectively. Derivation of the finite difference equations are given in Appendix B. Equation 3.4c

is then discretized at every point to evaluate the residuals in Equation 3.7

$$\mathbf{res} = \begin{bmatrix} \mathbf{g}_0(\mathbf{c}) \\ \mathbf{g}_1(\mathbf{c}) \\ 3(\mathcal{D}_T\mathbf{F}0 - v)\cdot\mathbf{T} + (\mathcal{D}_M\mathbf{F}0 - v)\cdot\mathbf{M} - v(3T^0 + M^0) \\ 3(\mathcal{D}_T\mathbf{E}\text{in} - v\mathbf{F}\text{in})\cdot\mathbf{T} + (\mathcal{D}_M\mathbf{E}\text{in} - v\mathbf{F}\text{in})\cdot\mathbf{M} - k_0\mathbf{A} \\ 3(\mathcal{D}_T\mathbf{F}N)\cdot\mathbf{T} + (\mathcal{D}_M\mathbf{F}N)\cdot\mathbf{M} \end{bmatrix} \tag{3.7}$$

where the third and fifth equations are the residuals for the boundary conditions at the start ($\zeta = 0$) and end ($\zeta = 1$) of the deposition zone respectively. $\mathbf{F}0$ is the first vector row in array $\mathbf{F}$ where the weights are calculated using forward finite differences. This vector is used to calculate the residual of the boundary condition at $\zeta = 0$ for $\mathbf{c}^{0^+}$ in Table 3.3 (see Figure 3.4) which is the third element in the residuals vector of Equation 3.7. $\mathbf{F}0$ is written as:

$$\mathbf{F}0 = \begin{bmatrix} \mathbf{F}(0,0) & \mathbf{F}(0,1) & \mathbf{F}(0,2) & \cdots & 0 \end{bmatrix}$$

where

$$\begin{aligned} \mathbf{F}(0,0) &= \frac{(\zeta_1 - \zeta_0)^2 - (\zeta_2 - \zeta_0)^2}{\xi_{\mathbf{F}0}} \\ \mathbf{F}(0,1) &= \frac{(\zeta_2 - \zeta_0)^2}{\xi_{\mathbf{F}0}} \\ \mathbf{F}(0,2) &= -\frac{(\zeta_1 - \zeta_0)^2}{\xi_{\mathbf{F}0}} \end{aligned}$$

with

$$\xi_{\mathbf{F}0} = (\zeta_1 - \zeta_0)^2 - (\zeta_2 - \zeta_0)(\zeta_1 - \zeta_0)^2 .$$

The matrix $\mathbf{F}$in is a matrix with the weights of the discretization of the first deriva-

tive at each interior collocation point. A vector row i of **F**in is given by

$$\begin{aligned}
\mathbf{F}(i, i-1) &= \frac{(\zeta_{i+1} - \zeta_i)^2}{\xi_{\mathbf{F}}} \\
\mathbf{F}(i, i) &= \frac{(\zeta_{i-1} - \zeta_i)^2 - (\zeta_{i+1} - \zeta_i)^2}{\xi_{\mathbf{F}}} \\
\mathbf{F}(i, i+1) &= \frac{-(\zeta_{i-1} - \zeta_i)^2}{\xi_{\mathbf{F}}}
\end{aligned}$$

where

$$\xi_{\mathbf{F}} = (\zeta_{i-1} - \zeta_i)(\zeta_{i+1} - \zeta_i)^2 - (\zeta_{i+1} - \zeta_i)(\zeta_{i-1} - \zeta_i)^2$$

Fin is the equivalent of **E**in for the discretization weights of the second derivative for the interior collocation points. The weights of **E**in for $i = 1, 2, \cdots, N$ are as follows

$$\mathbf{E}\text{in}_i = \begin{bmatrix} 0 & \cdots & \mathbf{E}(i, i-1) & \mathbf{E}(i, i) & \mathbf{E}(i, i+1) & \cdots & 0 \end{bmatrix} \qquad i = 1, \cdots, N$$

where central finite differences were used to calculate the weights as follow

$$\begin{aligned}
\mathbf{E}(i, i-1) &= \frac{(\zeta_{i+1} - \zeta_i)}{\xi_{\mathbf{E}}} \\
\mathbf{E}(i, i) &= \frac{(\zeta_{i-1} - \zeta_i) - (\zeta_{i+1} - \zeta_i)}{\xi_{\mathbf{E}}} \\
\mathbf{E}(i, i+1) &= \frac{-(\zeta_{i-1} - \zeta_i)}{\xi_{\mathbf{E}}}
\end{aligned}$$

and

$$\xi_{\mathbf{E}} = \frac{(\zeta_{i+1} - \zeta_i)(\zeta_{i-1} - \zeta_i)^2 - (\zeta_{i-1} - \zeta_i)(\zeta_{i+1} - \zeta_i)^2}{2}.$$

The vector **F**N is the last vector row of the **F** array. We use this vector to calculate the boundary condition at $\zeta = 1$ (column for $\mathbf{c}^1$ in Table 3.3). The vector has the form

$$\mathbf{F}N = \begin{bmatrix} 0 & \cdots & \mathbf{F}(N, N-2) & \mathbf{F}(N, N-1) & \mathbf{F}(N, N) \end{bmatrix}$$

for this vector the weights are calculated with a backward finite difference to obtain

$$\begin{aligned}
\mathbf{F}(N, N-2) &= \frac{-\left(\zeta_{N-2}-\zeta_{N-1}\right)^2}{\xi_{\mathbf{F}N}} \\
\mathbf{F}(N, N-1) &= \frac{\left(\zeta_{N-3}-\zeta_{N-1}\right)^2}{\xi_{\mathbf{F}N}} \\
\mathbf{F}(N, N) &= \frac{\left(\zeta_{N-2}-\zeta_{N-1}\right)^2-\left(\zeta_{N-3}-\zeta_{N-1}\right)^2}{\xi_{\mathbf{F}N}}
\end{aligned}$$

with

$$\xi_{\mathbf{F}N} = \left(\zeta_{N-2}-\zeta_{N-1}\right)\left(\zeta_{N-2}-\zeta_{N-1}\right)^2-\left(\zeta_{N-3}-\zeta_{N_1}\right)\left(\zeta_{N-2}-\zeta_{N-1}\right)^2.$$

$\mathbf{M} = [M_0, M_1, M_2, ..., M_N]^T$ are the discrete values of [M] at each collocation point in space; similarly $\mathbf{T}$, and $\mathbf{A}$ are the discretized values of [T] and [A] at each collocation point. Finally $\mathbf{c} = [\mathbf{M}, \mathbf{T}, \mathbf{A}]^T$. The residual (3.7) function was solved using a Newton-Raphson method with $N = 200$ collocation points with a tolerance of $tol < 10^{-12}$ for the norm of the residual. The resulting profiles are shown in Figure 3.5 where it can be observed that the adsorption of the monomer on the surface dominates the deposition and there is little trimer produced along the reactor, as is expected by the thermodynamic and kinetic values employed in the simulation.

The plot in the upper part of Figure 3.3 shows the an analysis of the residuals for a solution with $N = 200$. The linear behavior in the logarithmic scales (the norm of residuals axis is in logarithmic scale) indicates that our system exhibits superlinear convergence with an order of converge of -1.626. To analyze converge with respect to discretization level, we compare solutions with different number of collocation points against an analytical solution, or if an analytical solution is not available, we compare against a fine grid solution. The number of collocation points

for each grid is calculated as $N_i = 2_i^n + 1$ where $n_i = 2, 3, 4, \cdots$ to generate grids with matching collocation points and allow direct comparison of the function evaluations at the same spatial location. Since an analytical solution is not available, we consider a grid with $N_i = 2^{11} + 1 = 2049$ collocation points to be our fine grid. The error for a solution with N_i collocation points was computed as the norm of the difference vector $\mathbf{error} = \mathbf{y}_{fine} - \mathbf{y}_{N_i}$. The result of the analysis can be seen in the lower part of Figure 3.3, where the linear behavior of the residuals in both logarithmic scale axes allows to compute an order of converge as the slope of the curve to be -2.635.

Finally to investigate the time evolution of the surface property $\mathrm{L}(\zeta, \tau)$, in this case film thickness, $L(\zeta, \tau)$ is integrated at every collocation point in the slow time scale using Equation 3.4d to obtain the profile in Figure 3.6, where it has been integrated over 100 τ units ($\mathrm{m^3s/\#}$). Figure 3.6 shows the film thickness along the reactor spatial coordinate, ζ at different τ times. Since in the slow time the concentration profiles for precursors and adsorbed species are at quasi equilibrium, the time integration of L consist of solving a simple set of ordinary differential equations with a constant value (in time, but of course not in space) of $[A]$ at every collocation point. It can observed, that as expected, the thickness will grow more quickly near the entrance of the reactor where the concentration of the adsorbed species A is higher.

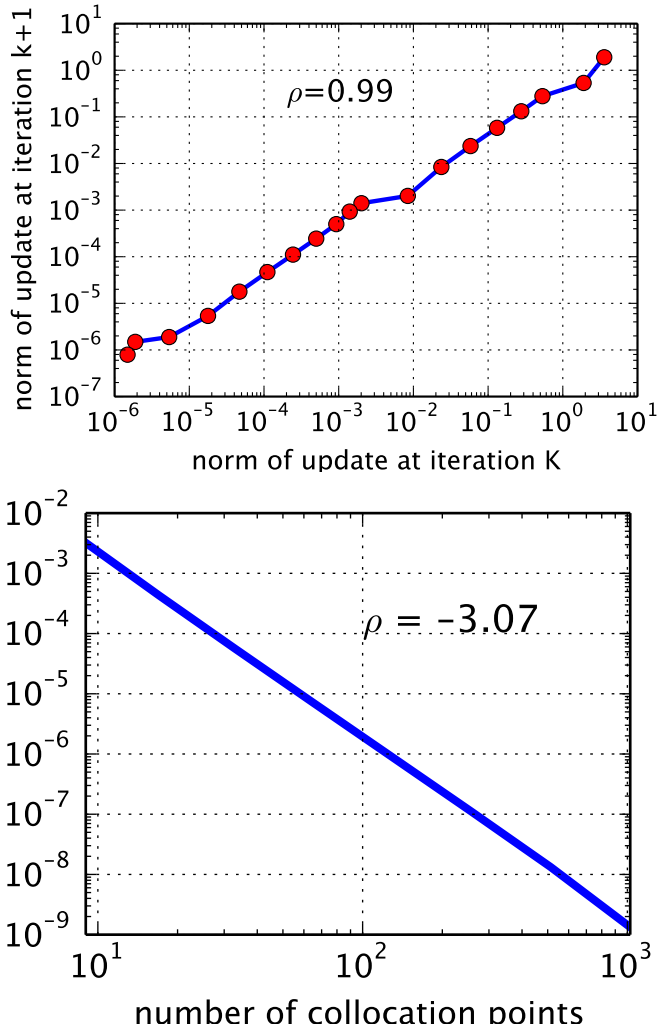

Figure 3.3: *Upper plot: Residuals during the spatial integration of the DAE system (3.4) showing a superlinear convergence order of -1.626 (the norm of residual axis is in logarithmic scale). Lower plot: Grid convergence analysis of the solution to the system in (3.4) (the error axis is in logarithmic scale) with an order of convergence of -2.635.*

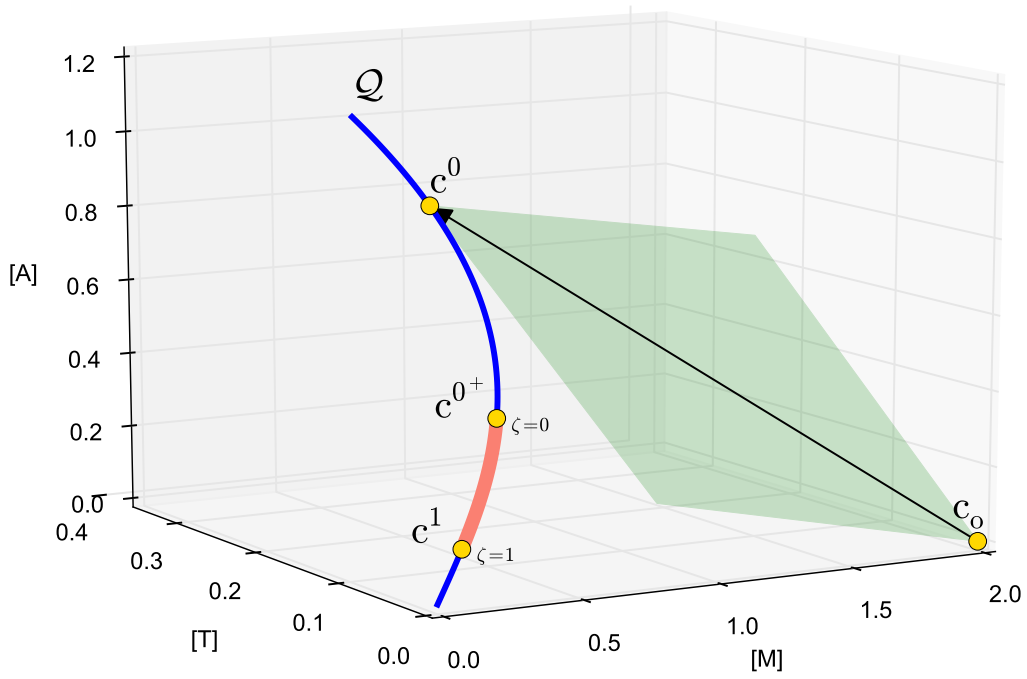

Figure 3.4: *Phase space plot of the system. The equilibrium manifold $\mathcal{Q}$ is shown as the solid blue curve and the spatial evolution of the system is graphed as the light red section along the manifold; each point in this section represents the composition in the reactor at a different point in space ζ. The boundary conditions are indicated by the yellow points. For reference on these conditions see Figure 3.1. The green plane represents constant x_0, i.e. precursor conservation and so any c_o in this plane will be projected to c^0 as a result of conservation of species.*

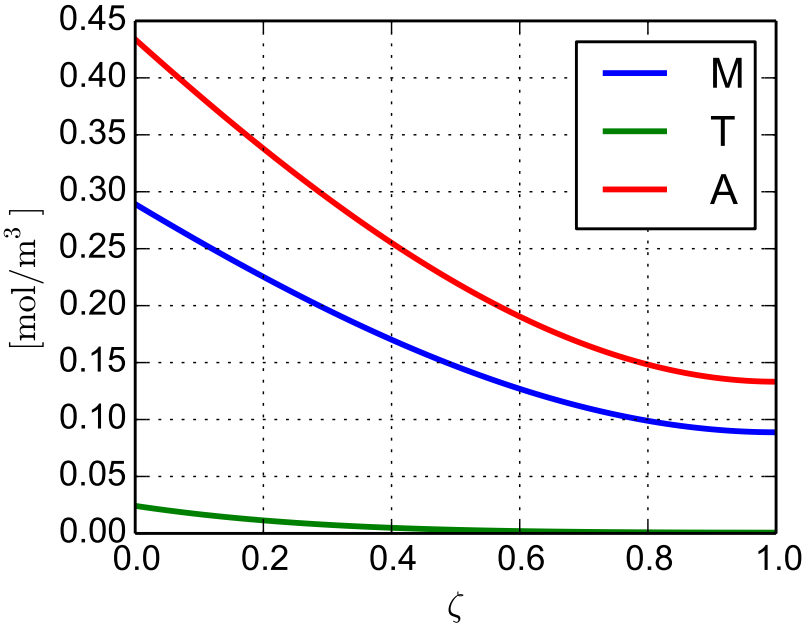

Figure 3.5: *Profiles of the concentration of monomer, [M], trimer, [T], and adsorbed, [A], species along the reactor length* ζ.

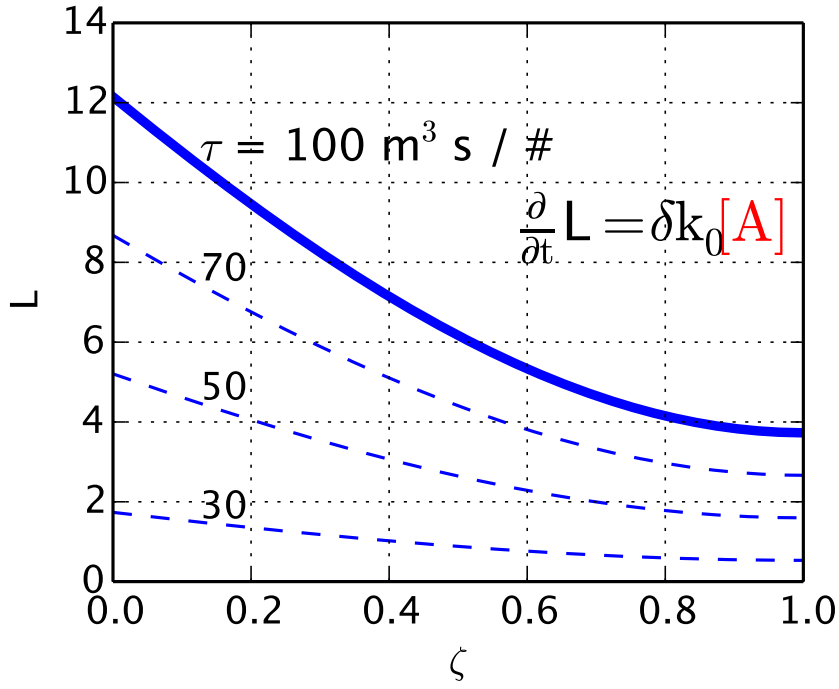

Figure 3.6: *Integrated profile of the surface property L, film thickness in this example, along the reactor coordinate* ζ *at different* τ *times.*

Chapter 4

Application of the factorization approach to copper CVD

This chapter describes the application of the reaction factorization methodology presented in previous chapters to the modeling of a hot wall chemical vapor deposition reactor. The factorization is shown to be able to guide the time scale separation and to reveal conserved quantities in the new reaction coordinates.

4.1 Copper chemical vapor deposition (Cu-CVD)

This section presents the application of the reaction factorization methodology to modeling of the chemical vapor deposition of copper for the reaction

$$\mathrm{CuI}(g) \rightarrow \mathrm{Cu}(s) + \frac{1}{2}\mathrm{I}_2(g)$$

in the reactor shown in Figure 4.1. Experiments on copper CVD and visual analysis of deposited films are presented in Appendix B. From the experimental and digital

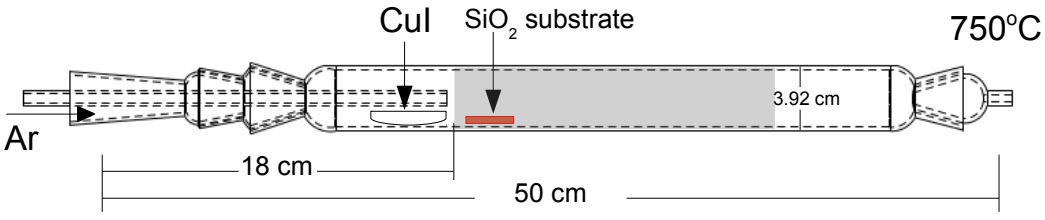

Figure 4.1: *Schematic of the hot wall tubular CVD reactor. The inner tube is not used for this deposition process. Argon flows through the outer tube.*

image analysis to be presented in Chapter 6, a single-island growth was inferred and

is explained as follows: first, Figure 4.2 shows that the film grows mostly through the formation, expansion and coarsening of islands, exhibiting a Volmer-Weber growth mode. Presumably, this occurs because the copper adatoms are more attracted to themselves than to the quartz surface, as suggested by the adsorption energies of copper on copper (1.25 eV [30]) and copper on quartz (0.1 eV [31]). Hence, it is assumed that the islands grow through two main precursor incorporation mechanisms: 1) by direct precursor impingement from the gas phase onto the growing Cu crystals; and 2) by initial adsorption onto the quartz, followed by surface diffusion of the adsorbed species to the growing Cu crystals.

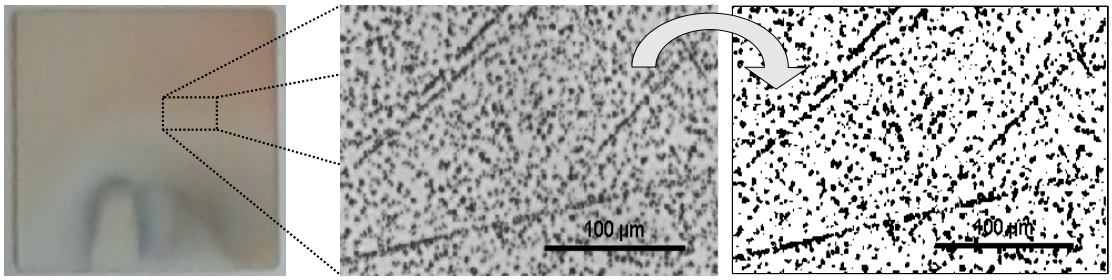

Figure 4.2: *Image analysis process of copper films deposited on quartz substrates using CuI as as copper precursor. The image on the left is a picture of the copper (red) deposited on a 1 inch by 1 inch quartz substrate. The image at the center is a optical microscope image of an area of the film. The image on the right is the digitally process image of the optical microscope image at the center. The processing was realized by filtering the microscope image digitally through a threshold value of 127 in the RGB color scale (the middle of the scale from 0(black) to 255(white) and converting it to black and white. Note the accumulation of copper clusters on the scratches of the film where the larger clusters form, a potential indicator of a surface reaction deposition mechanism.*

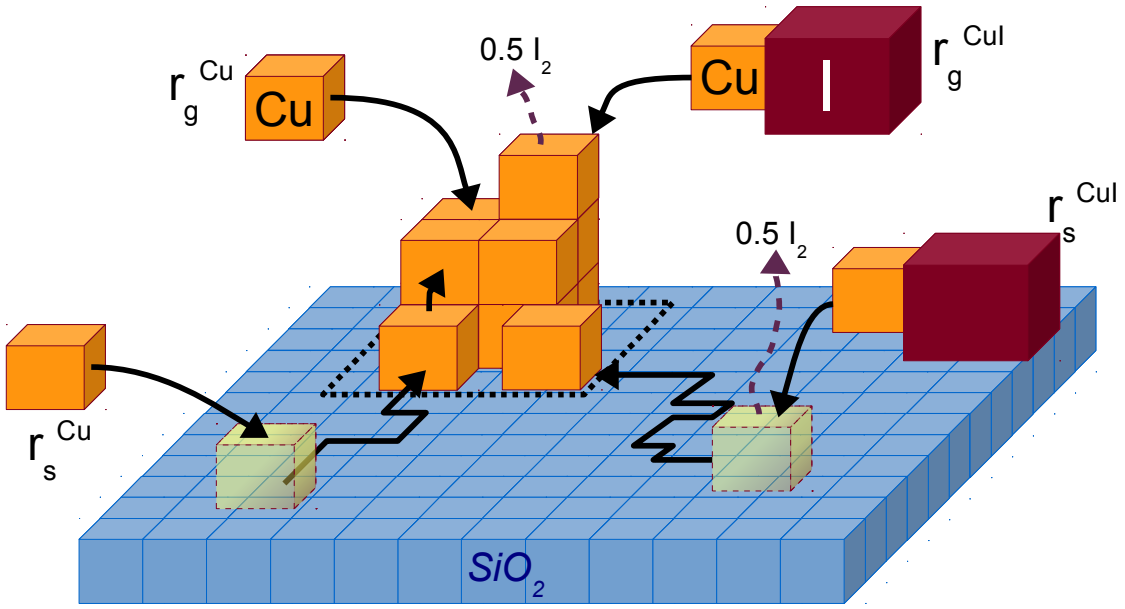

Figure 4.3: *Sketch of the proposed growth mechanism. Gold color cubes represent copper atoms and red cubes iodine atoms. Copper can be incorporated to a growing island through direct impingement of precursor molecules, Cu and CuI, from the gas phase, or through surface diffusion of copper adatoms (yellow color).*

4.1.1 Surface reactions and growth model

Figure 4.3 shows a schematic representation of a proposed copper crystal growth mechanism in which precursor incorporation occurs by two main processes: direct impingement from the gas phase, and surface diffusion of precursors deposited on the substrate surface. In the first process, r_g^{Cu} and r_g^{CuI}, copper and copper iodide from the gas phase deposit directly on the the growing islands, resulting in the addition of copper to the islands and the production of iodine. In the analysis that follows, it is assumed that iodine atoms adsorbed on the Cu surface combine instantly to form molecular iodide that immediately desorbs. The rate of this deposition mechanism by direct impingement from the gas phase can be estimated by the wall collision rates for gas phase Cu and CuI atoms using the kinetic theory of gases and assuming an ideal gas

$$r_g^{Cu} = \eta_{Cu}\sqrt{\frac{k_B T}{2\pi m_{Cu}}}\,[Cu]\,A_g, \qquad r_g^{CuI} = \eta_{CuI}\sqrt{\frac{k_B T}{2\pi m_{CuI}}}\,[CuI]\,A_g \tag{4.1}$$

where k_B is the Boltzmann constant, η_i is the sticking coefficient of precursor i, m_{Cu} is the mass of a copper atom, m_{CuI} is the mass of a copper iodide molecule, $[Cu]$ and $[CuI]$ are the gasp-phase concentrations of copper and copper iodide, respectively, and A_g is the surface area available for deposition. To estimate this area, we consider the islands to grow in a cubic manner. Therefore, for an island with n_{Cu} atoms of copper, the length of the side of the island is $L = n_{Cu}^{1/3} L_{Cu}$ where $L_{Cu} = 0.228$ nm is the length of a solid copper atom represented as a cube. Then the area available for deposition on the island is given by the following equation

$$A_g = 5 \times (L)^2 \tag{4.2}$$

In the second mechanism the copper atoms deposit and weakly bond to the quartz surface. These adatoms diffuse on the surface until they encounter the edge of a growing island and are adsorbed by it. To estimate the rate of this adsorption process through surface diffusion, absolute rate theory [32] is used to obtain equations 4.3 and 4.4, representing the rates of adsorption of Cu and CuI on the quartz surface

$$r_s^{Cu} = \frac{k_B T}{h} \theta_{Cu/SiO_2} [\hat{X}] K_{ads}^{Cu} A_{edge} \tag{4.3}$$

$$r_s^{CuI} = \frac{k_B T}{h} \theta_{CuI/SiO_2} [\hat{X}] K_{ads}^{CuI} A_{edge} \tag{4.4}$$

where h is Plank's constant, $\theta_{Cu/SiO2}$ is the equilibrium fraction coverage of copper on quartz at the deposition temperature, $[\hat{X}]$ is the surface site density of copper on quartz, and A_{edge} is the area of edge sites available on the surface. The area

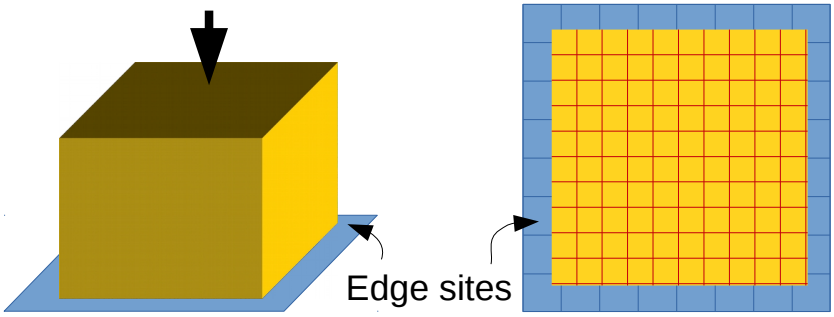

Figure 4.4: *Sketch of the top view of the area around the edge of the growing Cu crystal (in yellow) on a quartz surface (in light blue).*

of edge sites, shown in Figure 4.4, available for deposition is estimated as follows: first the number of copper sites in a side of the base of the island is calculated as $n_{Cu_{side}} = (L/L_{Cu} + 1)$. Second the total area available for the sites on the perimeter of the base is estimated as $A_{peri} = n_{Cu_{side}} v_{Cu_1}^{2/3}$, where Cu_1 is the volume of a solid

atom of copper. Finally to estimate the equivalent area of SiO_2 surface sites, the calculated copper edge area is divided by the area of a quartz surface site.

$$A_{edge} = \frac{4\left(\frac{L}{L_{Cu}} + 1\right)}{\hat{X}} \frac{v_{Cu_1}^{2/3}}{v_{SiO2}^{2/3}}$$

To track the growth of the islands, we use the model given in Equation 4.5.

$$\frac{dL}{dt} = \delta\left(r_g^{Cu} + r_s^{Cu} + r_g^{CuI} + r_s^{CuI}\right) \tag{4.5}$$

This completes the surface adsorption and growth model components.

4.1.2 Gas phase reactions

To calculate the concentration of precursors in the gas over the substrate surface the following reactions are considered: (1) the reversible reaction between the monomer CuI and the Cu_3I_3 trimer and (2) the reversible reaction between gas phase atomic Cu and the Cu_2.

The complete mechanism is shown in Figure 4.5, where D(s) represents an surface adsorption site (either copper or quartz) and D(s)−Cu is an adsorbed copper atom. The reactions and their rate expressions are presented in Table 4.1. In the table, lower case k represents a forward reaction constant and upper case K an equilibrium constant. The calculations of the adsorption and equilibrium constants are detailed in Chapter 5.

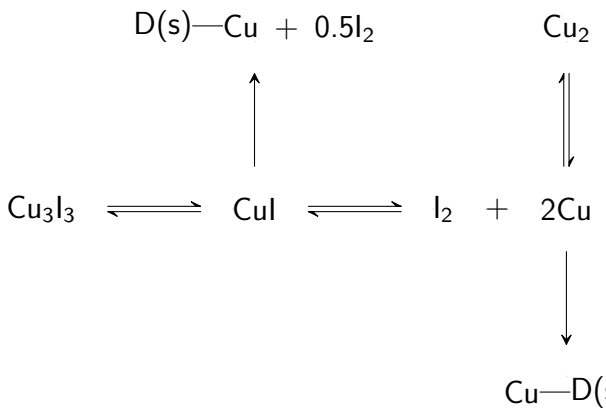

Figure 4.5: *The gas-phase reactions and their connection to the deposition process.* $D(s)$ *is a deposition site that can be either a copper surface site or a quartz surface site. All species are gas phase species unless noted as surface (s) species.*

0)	$3CuI$	$\overset{k_0 K_0}{\underset{k_0}{\rightleftharpoons}}$	Cu_3I_3	$r_0 = \frac{1}{\epsilon_0}\left(K_0\left[CuI\right]^3 - \left[Cu_3I_3\right]\right)$
1)	$2CuI$	$\overset{k_1 K_1}{\underset{k_1}{\rightleftharpoons}}$	$Cu_2 + I_2$	$r_1 = \frac{1}{\epsilon_1}\left(K_1\left[CuI\right]^2 - \left[Cu_2\right]\left[I_2\right]\right)$
2)	Cu_2	$\overset{k_2 K_2}{\underset{k_2}{\rightleftharpoons}}$	$2Cu$	$r_2 = \frac{1}{\epsilon_2}\left(K_2\left[Cu_2\right] - \left[Cu\right]^2\right)$
3)	Cu	$\overset{r_3}{\rightarrow}$	$D(s)$	$r_3 = r_g^{Cu}\left(\left[Cu\right]\right) + r_s^{Cu}\left(\left[Cu\right]\right)$
4)	CuI	$\overset{r_4}{\rightarrow}$	$D(s) + \frac{1}{2}I_2$	$r_4 = r_g^{CuI}\left(\left[CuI\right]\right) + r_s^{CuI}\left(\left[CuI\right]\right)$

Table 4.1: *The mechanism considered for Cu deposition from CuI. Reactions 1 through 3 are assumed to have relatively fast dynamics, where as reactions 4 and 5 the deposition reactions are considered to be the rate-limiting steps, and* $\epsilon_i = 1/k_i$ *for* $i = 0, 1, 2$.

4.1.3 Precursor depletion spatial profiles in the hot-wall tubular CVD reactor

To compute the depletion behavior of the copper-containing precursors during deposition, consider the reactor schematic in Figure 4.1 where the shaded area represents where deposition is observed during experiments. The analysis in this section assumes the gas flowing in the reactor to follow the plug flow model with no diffusion. It is also assumed that there are no gas-phase composition gradients in the radial direction. To derive the governing equations for this model, consider the sketch in Figure 4.6 that models the interior of the reactor in Figure 4.1 where

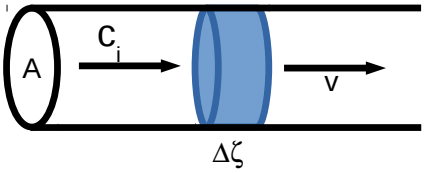

Figure 4.6: *Plug flow sketch for the precursor depletion model.*

$A = \pi R_o^2$ is the area normal to the flow and $R_o = 1.95 \times 10^7 nm$ is the inner radius of the reactor tube, c_i is the precursor species i concentration, $v = 3 \times 10^7$nm/s (resulting from 570 sccm of Ar flowing at 750°C) is the fluid velocity, and $V_\zeta = \pi R_o^2 \Delta\zeta$ is the volume of the differential element of Figure 4.6. A mass balance over the differential volume yields the following equation

$$\pi R_o^2 \Delta\zeta \frac{\partial \mathsf{c}_i}{\partial t} = \pi R_o^2 \mathsf{c}_i|_\zeta \nu - \pi R_o^2 \mathsf{c}_i|_{\zeta+\Delta\zeta} \nu + \pi R_o^2 \Delta\zeta \mathsf{r}_i(\mathsf{c}) \qquad i = 0, 1, .., 4$$

where r_i is the overall rate of consumption of precursor i according to the rate expressions of Table 4.1 and ν is the average flow velocity. Dividing by the differential

volume and taking the limit when $\Delta\zeta \to 0$ we obtain the deposition model

$$\frac{\partial \mathbf{c}}{\partial t} = -\nu \frac{\partial \mathbf{c}}{\partial \zeta} + \mathbf{r}(\mathbf{c}) \tag{4.6}$$

where $\mathbf{c}$ and $\mathbf{r}$ are the vectors of concentration of species and reaction rate expressions, respectively, as shown below

$$\mathbf{c} = \begin{bmatrix} [Cu_3I_3] \\ [I_2] \\ [Cu] \\ [CuI] \\ [Cu_2] \end{bmatrix} \qquad \mathbf{r} = \begin{bmatrix} r_0 \\ r_1 + 0.5r_4 \\ 2r_1 - 2r_2 - \sigma r_3 \\ -3r_0 - 2r_1 - \sigma r_4 \\ r_2 \end{bmatrix}.$$

Note that for the deposition reactions, r_3 and r_4 in Table 4.1, the rate expressions must to be multiplied by the following surface area to volume ratio to match the units of the differential volume derivation

$$\sigma = \frac{A}{V} = \frac{2\pi R_o v}{\pi R_o^2 v} = \frac{2}{R_o}.$$

Including the reaction for tracking the average island size (4.5), the time-dependent distributed deposition system is modeled by the following equations

$$\frac{\partial}{\partial t}\begin{bmatrix} [Cu_3I_3] \\ [I_2] \\ [Cu] \\ [CuI] \\ L \\ [Cu_2] \end{bmatrix} = -v\frac{\partial}{\partial \zeta}\begin{bmatrix} [Cu_3I_3] \\ [I_2] \\ [Cu] \\ [CuI] \\ 0 \\ [Cu_2] \end{bmatrix} + \begin{bmatrix} 1 & 0 & 0 & 0 & 0 & 0 \\ 0 & 1 & 0 & 0 & \sigma/2 & 0 \\ 0 & 2 & -2 & -\sigma & 0 & 0 \\ -3 & -2 & 0 & 0 & -\sigma & 0 \\ 0 & 0 & 0 & 0 & 0 & 1 \\ 0 & 0 & 1 & 0 & 0 & 0 \end{bmatrix}\begin{bmatrix} r_0 \\ r_1 \\ r_2 \\ r_3 \\ r_4 \\ r_5 \end{bmatrix} \tag{4.7}$$

where

$$r_5 = \delta \left(r_g^{Cu} + r_s^{Cu} + r_g^{CuI} + r_s^{CuI} \right)$$

from Equation 4.5, where $\delta \ll 1$ is a small parameter that represents the ratio of the deposition time scale to the species transport time scale, as discussed in Chapter 3, and it can be estimated as $\delta =$ reactor residence time/total deposition time.

4.1.4 Application of the reaction factorization

We apply the reaction factorization developed in Chapters 2 and 3 to the reaction system (4.7) to eliminate redundant dynamic modes and to allow ϵ_0,ϵ_1,$\epsilon_2 \to 0$, transforming the system into the standard singular perturbation form. The new reaction coordinates resulting from the reaction factorization are given in Equa-

tion 4.8.

$$\mathbf{y} = \mathbf{U} \cdot \mathbf{c} = \begin{bmatrix} 1 & 0 & 0 & 0 & 0 & 0 \\ 0 & 1 & 0 & 0 & 0 & 0 \\ 0 & 0 & 0 & 0 & 0 & 1 \\ 0 & 2 & -1 & 0 & 0 & -2 \\ 0 & 0 & 0 & 0 & 1 & 0 \\ 3 & 2 & 0 & 1 & 0 & 0 \end{bmatrix} \cdot \mathbf{c} \tag{4.8}$$

$$\mathbf{y} = \begin{bmatrix} [Cu_3I_3] \\ [I_2] \\ [Cu]_2 \\ 2[I_2] - [Cu] - 2[Cu_2] \\ L \\ 3[Cu_3I_3] + [CuI] + 2[I_2] \end{bmatrix} = \begin{bmatrix} z_0 \\ z_1 \\ z_2 \\ x_0 \\ x_1 \\ w_0 \end{bmatrix}$$

Multiplying the system of ODEs in (4.7) by the transformation matrix $\mathbf{U}$ yields the singular perturbation problem

$$\frac{\partial}{\partial t}\begin{bmatrix} z_0 \\ z_1 \\ z_2 \\ x_0 \\ x_1 \\ w_0 \end{bmatrix} = -v\frac{\partial}{\partial \zeta}\begin{bmatrix} z_0 \\ z_1 \\ z_2 \\ x_0 \\ 0 \\ w_0 \end{bmatrix} + \begin{bmatrix} 1 & 0 & 0 & 0 & 0 & 0 \\ 0 & 1 & 0 & 0 & \sigma/2 & 0 \\ 0 & 0 & -2\sigma & 0 & 0 & 0 \\ 0 & 0 & 0 & \sigma & \sigma & 0 \\ 0 & 0 & 0 & 0 & 0 & 1 \\ 0 & 0 & 0 & 0 & 0 & 0 \end{bmatrix}\begin{bmatrix} \frac{1}{\epsilon_0}g_0 \\ \frac{1}{\epsilon_1}g_1 \\ \frac{1}{\epsilon_2}g_2 \\ f_3 \\ f_4 \\ \delta f_5 \end{bmatrix}$$

where

$$\begin{aligned} g_0 &= K_0 \left[\mathrm{CuI}\right]^3 - \left[\mathrm{Cu_3I_3}\right] \\ g_1 &= K_1 \left[\mathrm{CuI}\right]^2 - \left[\mathrm{Cu_2}\right]\left[\mathrm{I_2}\right] \\ g_2 &= K_2 \left[\mathrm{Cu_2}\right] - \left[\mathrm{Cu}\right]^2 \\ f_3 &= r_g^{Cu}\left([Cu]\right) + r_s^{Cu}\left([Cu]\right) \\ f_4 &= r_g^{CuI}\left([CuI]\right) + r_s^{CuI}\left([CuI]\right) \\ f_5 &= r_g^{Cu} + r_s^{Cu} + r_g^{CuI} + r_s^{CuI} \end{aligned}$$

Taking the limit $\epsilon_i \to 0$ for $i = 0, 1, 2$ and $\delta \to 0$ to obtain the DAE system

$$\begin{aligned} g_0 &= 0 \\ g_1 &= 0 \\ g_2 &= 0 \\ \frac{\partial x_0}{\partial t} &= -v\frac{\partial x_0}{\partial \zeta} + \sigma f_3 + \sigma f_4 \\ \frac{\partial x_1}{\partial t} &= f_5 \\ \frac{\partial w_0}{\partial t} &= -v\frac{\partial w_0}{\partial \zeta} \end{aligned} \tag{4.9}$$

We define the slow time scale $\tau = \delta t$ in which the deposited film property evolves (see Section 3 in Chapter 3) and let $\delta \to 0$ to obtain

$$\begin{aligned} g_0 &= 0 \\ g_1 &= 0 \\ g_2 &= 0 \\ \frac{dx_0}{d\zeta} &= -\frac{\sigma}{v}(f_3 + f_4) \\ \frac{dx_1}{d\tau} &= f_5 \quad (*) \\ \frac{dw_0}{d\zeta} &= 0 \end{aligned} \tag{4.10}$$

The separation of time scales is evident in this formulation from the following two observations: 1) there is one ODE (labeled *) in time, and 2) the pseudo equilibrium manifold is defined by a combination of equilibrium relationships and the gas phase transport/deposition equation. Furthermore, the conserved quantity w_0, which is the conservation of iodine across the reaction in the gas phase, is revealed through the reaction factorization

$$\frac{dw_0}{d\zeta} = \frac{d}{dt}\left(3\left[Cu_3I_3\right] + \left[CuI\right] + 2\left[I_2\right]\right) = 0 \quad \Rightarrow \quad w_0 = w_o$$

where $w_o = \mathbf{U}_w \mathbf{c}_o$ is the flux for the total number of iodine atoms at any point within the reactor at any point in time $t > 0$.

4.1.5 Integration of the DAE system

Before integrating the DAE system (4.10) resulting from the reaction factorization, we must pay special attention to the boundary condition at the start of

the deposition zone, well known as one of the main difficulties when solving DAE systems [27, 29]. Our initial and boundary conditions must not only satisfy the algebraic equations and the iodine species conservation relationship, but they must also satisfy boundary condition of pure convective flow at the inlet of the reactor for the gas phase transport equation in variable x_0,

$$\left.\frac{dx_0}{d\zeta}\right|_{\zeta=0} = 0 \quad \Rightarrow \quad 2\left[I_2\right]_0 - \left[Cu\right]_0 - 2\left[Cu_2\right]_0 = 0 \quad \Rightarrow \quad \frac{2\left[I_2\right]_0}{\left[Cu\right]_0 + 2\left[Cu2\right]_0} = 1$$

Note that this boundary condition in the new reaction coordinates preserves the ratio of total amount of Cu to I on CuI (the specified inlet condition) at the beginning of the deposition zone. Assuming the initial condition of an empty reactor, i.e. $\mathbf{c}(\zeta, 0) = 0$, we can now integrate the system (4.10) in time and space in the manner described below.

First the specified inlet conditions $\mathbf{c}_o$ are transformed into the new coordinate system to obtain $\mathbf{y}_o$

$$\mathbf{y}_o = \mathbf{U} \cdot \mathbf{c}_o.$$

Then we project these inlet conditions onto the equilibrium manifold $\mathcal{Q}$, to find the boundary condition at c^0 by solving the following set of equations

$$\begin{bmatrix} \mathbf{U}_x\mathbf{c}^0 \\ \mathbf{g}(\mathbf{c}^0) \\ \mathbf{U}_w\mathbf{c}^0 \end{bmatrix} = \begin{bmatrix} \mathbf{x}_o \\ \mathbf{0} \\ \mathbf{w}_o \end{bmatrix}.$$

where $\mathbf{U}_x$ = [2 -1 0 0 0 -2] and $\mathbf{U}_w$ = [3 2 0 1 0 0] are the rows of $\mathbf{U}$ corresponding to the new reaction coordinates x, and w, respectively. As noted in Chapter two we recall that even though the manifold $\mathcal{Q}$ is defined in the original reaction coordinates,

the above equation yields the projected initial conditions in the full new reaction coordinates space.

Next we compute the current spatial state of the system by integrating the new reaction coordinate associated with the slow mode, x_0, in space. To do this we follow an Euler implicit scheme to approximate the difference in space.

$$\frac{dx_0}{d\zeta} = \frac{x_0^{i+1} - x_0^i}{\Delta_\zeta}$$

where

$$\mathbf{x_0}^i = \mathbf{U}_{x_0} \cdot c^i$$

is the state if new coordinate x_0 at the current spatial integration step. Then we find the composition state of the system at the next step in space by solving the following system of equations using a Newton-Raphson technique.

$$\begin{bmatrix} \left(x_0^{i+1} - x_0^i\right)/\Delta_\zeta - \mathsf{f}\left(\mathbf{U}^{-1}\mathbf{y}^{i+1}\right) \\ \mathbf{g}\left(\mathbf{U}^{-1}\mathbf{y}^{i+1}\right) \\ \mathsf{w}_o - \mathsf{w}_0^{i+1} \end{bmatrix}.$$

After completing the integration in space, we use the new spatial state of the system to evaluet f_5 and realize a step integration of the ODE in time (labeled *) in Equation 4.10

4.1.6 Simulation results and discussion

At the beginning of the simulation we assume there is a number *nucSite* of nucleation sites containing a single copper atom each to initialize the island growth

model and estimate the surface deposition area at every time integration step. Table 4.2 shows the parameters for the nominal operation of the CVD hot-wall reactor used for experiments in Appendix A and Chapter 6. Figure 4.7 shows the spatial

Parameter	Value	Units
v	0.03	m/s
K_0	4.72×10^{11}	nm^6
K_1	1.23×10^{-14}	
K_2	1.09×10^{-7}	nm^{-3}
R_o	0.0195	m
T	750	°C
$[CuI]_o$	1.48×10^{-05}	nm^{-3}
η_{Cu}	5×10^{-03}	
η_{CuI}	5×10^{-04}	
m_{Cu}	1.05×10^{-25}	kg/atom
m_{CuI}	3.16×10^{-25}	kg/molecule
$nucSites$	4.15×10^{-7}	$\#/nm^2$

Table 4.2: *Parameters used in the simulation of CuCVD at nominal conditions 1 atm at 750°C . The boat in Figure 4.1 is loaded with 0.1 grams of copper iodide from which* $[CuI]_o$ *is estimated.*

concentration profiles of the precursors in the reactor. It can be seen that the concentration of the copper-containing species decreases as the deposition progresses along the length of the reactor, whereas the concentration of iodine molecules in the gas phase rises sharply driven by reactions r_4 and r_1. The concentration axis on the

plot in the bottom part of Figure 4.7 is in logarithmic scale to show species with very low concentrations.

The average size of the growing islands in the film is shown in Figure 4.8. At the beginning of the ten minute deposition period and in the area closer to the precursor boat, the concentration of the precursors is higher and thus more copper is deposited on the surface. The islands consequently grow larger in this zone. Downstream, the gasp phase concentration of precursors decreases at a reduced rate and thus the islands that form have a more uniform average size through the remainder of the reactor.

In Figure 4.9, we compare the direct (top) and surface diffusion (bottom) deposition rates of copper and copper iodide. Both rates exhibit the same decreasing trend due to the depletion of precursor species along the reactor. The depleted precursors result in smaller islands and thus less growth area, which in turn drives the deposition reactions to slower rates.

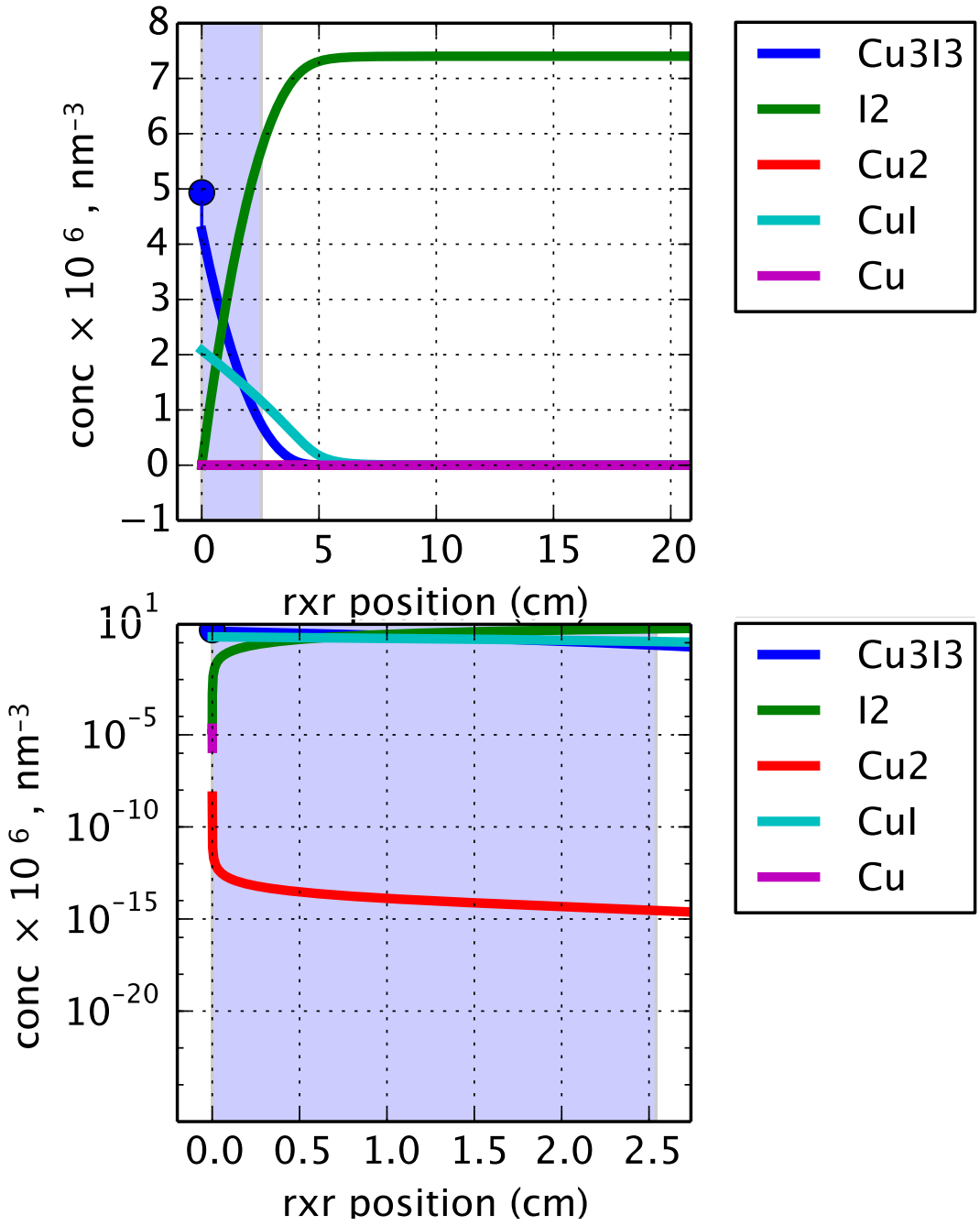

Figure 4.7: *Concentration profiles of precursors along the reactor. The spatial integration of the system is done on the deposition zone. This zone is the shaded area in the reaction schematic of Figure 4.1. The boundary condition at the beginning of the deposition zone is indicated by the filled circle in the copper iodide profile. The light blue shaded area is the physical position of the substrate on the reactor coordinate.*

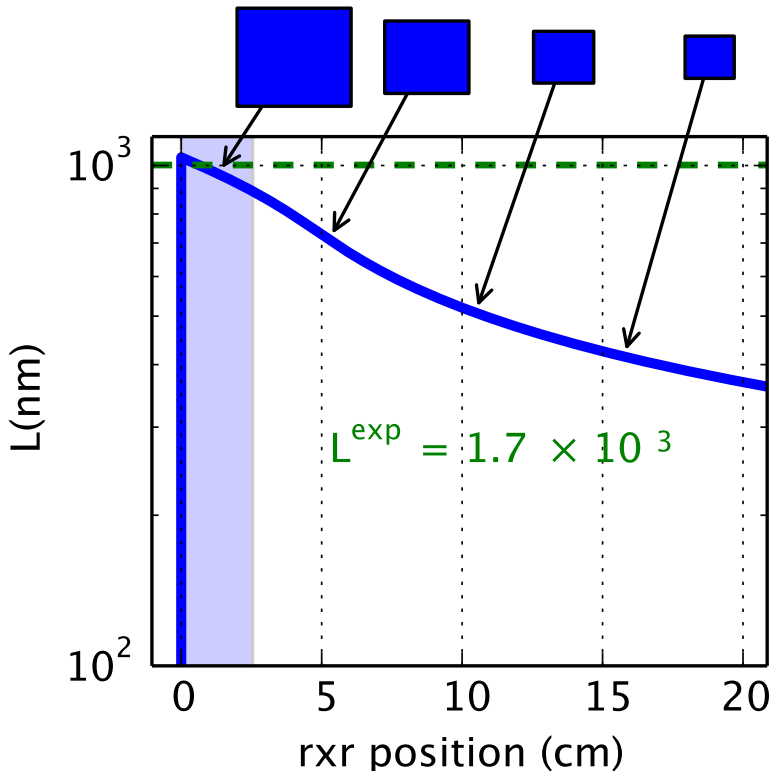

Figure 4.8: *Average island size in the growing film along the reactor dimension. The light blue shaded area is the physical position of the substrate in the reactor coordinate. Note that the model predicts the average size length of the islands to match the experimental average island size in the substrate.*

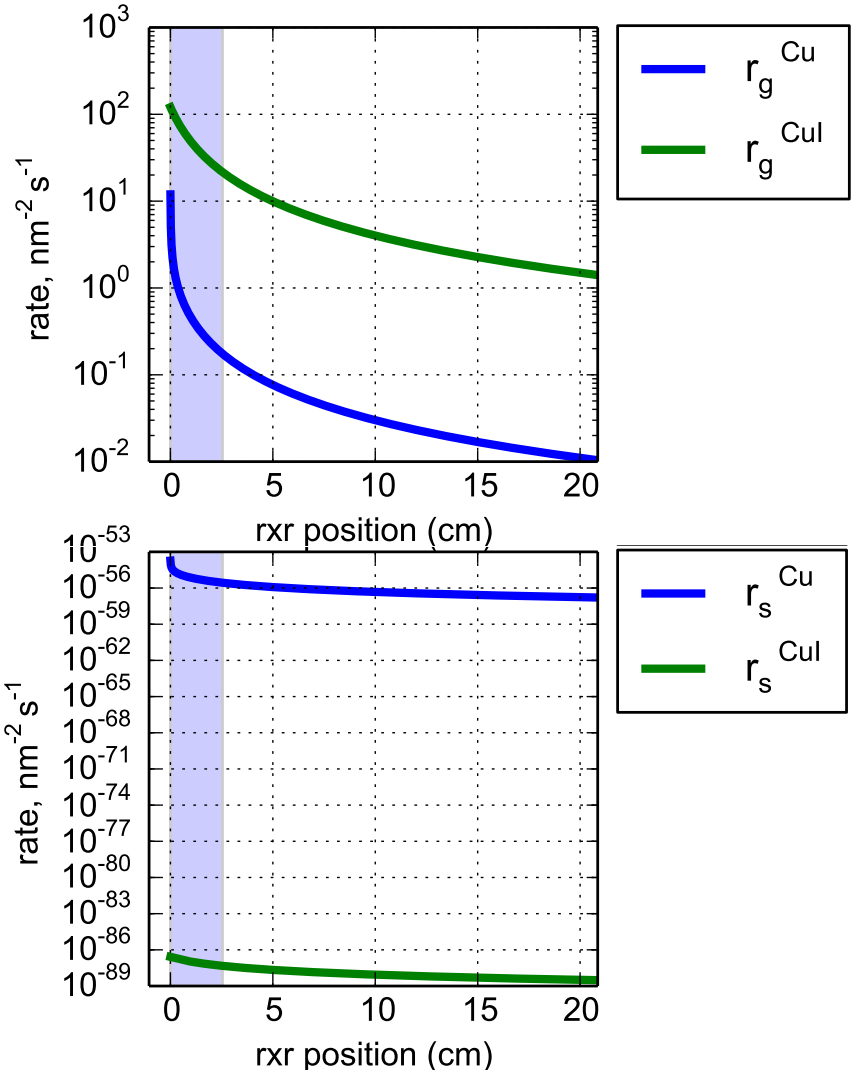

Figure 4.9: *A Snapshoot at time = 5 minutes of the deposition rates of copper and copper iodide on the surface of growing islands. The plot on the left compares direct deposition rates from the gas phase, and the plot on the right compares deposition rates by surface diffusion, The scale of the rate axes is logarithmic.*

Chapter 5

Numerical tools

This chapter describes numerical tools created to perform the absolute rate theory calculations used to estimate the adsorption isotherms and surface deposition rate constants of Chapter 4. The molecular properties of the species and the methods used to calculate partition functions are structured in object-oriented classes in the programming language PYTHON and are described in the following sections.

5.1 Chemical species class

A root class called **species** was created to store the universal constants Avo, k_B, h (Avogrado number, Boltzmann and Planck constants, respectively) to make them available for inheritance by sub-classes of specific species. While the library of classes continues to grow, the current classes can divided into two: 1) classes for gas phase species and 2) classes for adsorbed species.

The classes for the gas phase consist of mono-atomic and polyatomic (including diatomic) classes. The properties required to instantiate an object of the mono-atomic gas phase class are simply the molecular weight MW of the gas and the electronic energy modes. The electronic energy modes are obtained from tables of electronic energy states that list the energy level ξ_{el} and the degeneracy ω_{el}. The degeneracy is the number of different states (configurations) that have the same

energy level. This class contains methods to compute the partition function for the translational (`trans(T)`) and electronic (`elect(T)`) degrees of freedom at a given temperature `T`. Details of the derivation and calculation of the partition functions for this and all classes can be found in statistical thermodynamic references such as [33, 34].

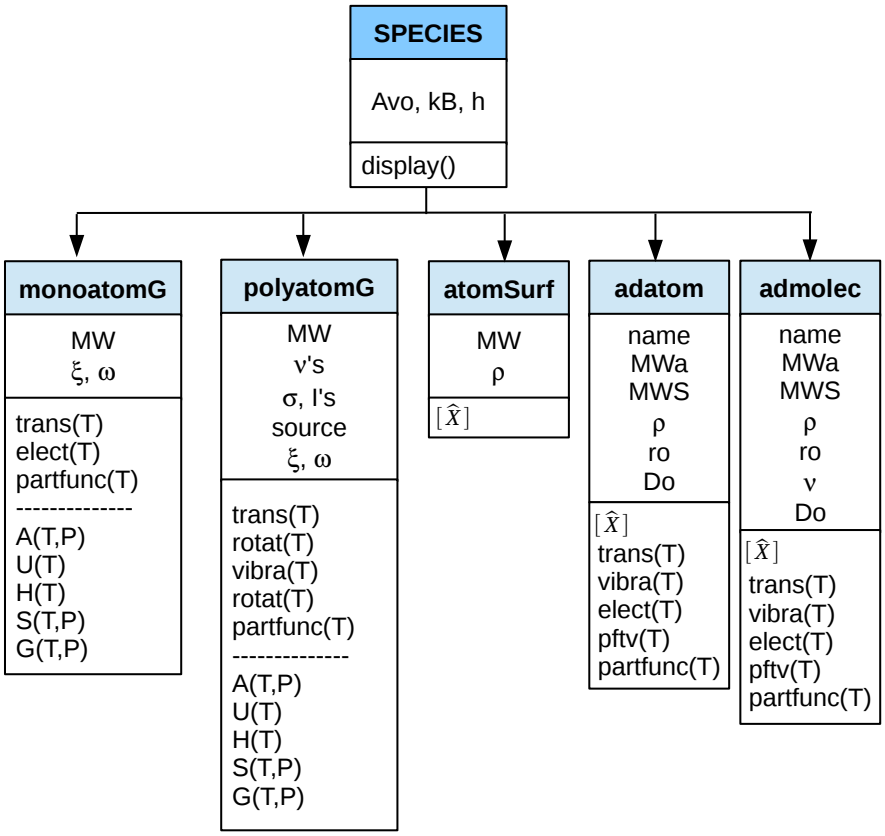

Figure 5.1: *Representation of the species classes.* ***`atomSurf`*** *is a simple class that represents a surface site, it requires only the molecular weight of the species, its density, and it calculates the site density* $[\hat{X}]$.

Gas phase species

The class for polyatomic gas phase species requires the vibrational frequencies (ν_i) the symmetry number σF and the moments of inertia I_i of the molecule (or rotation numbers if available in the CCCBDB/NIST [35] data base), in addition of the electronic energy levels, to be instantiated. If information to calculate the rotational energy modes is not available, the species class has another method to calculate the moments of inertia from the relative location of the atoms to each other in the molecule [36]. The polyatomic species class has methods to compute the partition functions for the main energy modes: transitional (`trans(T)`), rotational (`rota(T)`), vibrational (`vibra(T)`) and electronic (`elect(T)`).

Surface species

The classes for surface species that represent an adsorbed atom and an absorbed molecule, are adatom and admolec, respectively. They have common properties: MWa (molecular weight of the adsorbed species), MWS (molecular weight of the surface material), ρ density of the surface material and D_o the energy of the bond between the species and the surface. Both species classes have methods for computing the translational, vibrational, rotational and electronic partition functions. The vibrational mode perpendicular to the surface is estimated within the vibrational methods in both classes. For the admolec class, if the adsorbed molecule has vibrational modes other than the perpendicular, the frequencies ν's of these extra vibrational modes need to be supplied during the instantiation. The partition func-

tion calculations of these classes are used to estimate adsorption isotherms through absolute rate theory as discussed in the next section.

Figure 5.1 shows an schematic describing the different classes and subclasses for different the types of species in every block rectangle. For a particular block the first section under the name of the class shows the molecular properties required to define an object of such class. Then the second block under the name, shows the functions (methods) that such species supports. e.g. partition function calculations and thermodynamic state functions such as Helmholtz free energy A(T,P), internal energy U(T), enthalpy H(T), entropy S(T,P) and G(T,P). This thermodynamic state functions are calculated with the partition function methods, and where created to test the validity of the partition function methods in each species in the gas phase.

5.2 Adsorption isotherms from absolute rate theory

To estimate the adsorption isotherm and growth rates we follow Laidler *et. al.* [32] who applied the absolute rate theory to develop expressions for adsorption isotherms. Following their derivation, consider the deposition process illustrated in Figure 5.2 where a molecule of gas-phase species A deposits on a surface site X and forms the adsorbed species AX.

The equilibrium criterion at constant temperature yields the following expression

$$K_{eq} = \frac{[AX]}{[A]\,([X]-[AX])} = \frac{N_{AX}/S}{(N_A/V)\,(N_X/S)} = \frac{\mathcal{Z}_{AX}}{(\mathcal{Z}_A/V)\,\mathcal{Z}_X} \quad \text{with units } \mathrm{m}^3 \qquad (5.1)$$

where $\mathcal{Z}_{AX}$, $\mathcal{Z}_A$ and $\mathcal{Z}_X$ are the partition functions of the adsorbed species, the

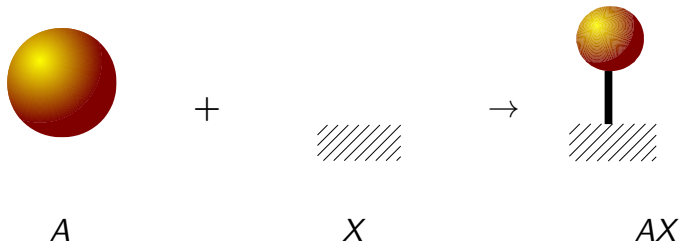

Figure 5.2: *Schematic of an adsorption reaction. A is the precursor molecule in the gas phase, X is a surface site available for deposition and AX is the adsorbed molecule A on the site X.*

molecule in the gas phase, and the surface site, respectively. $[A] = N_A/V$ is the concentration of the gas-phase species per unit volume. $[AX] = N_{AX}/S$ is the concentration of surface sites occupied by the adsorbed species and $[X] = N_X/S$ is the number of surfaces sites available for deposition. S is the area of a surface deposition site. Note that if $[\hat{X}]$ (sites/area) is the surface site density of the substrates, $S = 1/[\hat{X}]$.

5.2.1 Copper adsorption isotherm

To make this discussion more concrete, consider the deposition of gas-phase atomic copper on a copper or quartz substrate. The partition function of a copper atom in the gas phase will have only ground state electronic, $\mathcal{Z}_{A,0}$ and translational contributions, $\mathcal{Z}_{A,trans}$. Thus its partition function is

$$\mathcal{Z}_A/V = \mathcal{Z}_{A,trans}\mathcal{Z}_{A,0} = \left(\frac{2\pi m k_B T}{h^2}\right)^{3/2} \exp\left(\frac{-E_{Cu}}{k_B T}\right) \tag{5.2}$$

The adsorbed copper atom can move in only two directions and so loses one translational degree of freedom relative to the gas phase. However, there is an extra

vibrational degree of freedom perpendicular to the substrate. Hence its partition function is as follows

$$\begin{aligned} \mathcal{Z}_{AX} &= \mathcal{Z}_{AX,trans}\mathcal{Z}_{AX,vib}\mathcal{Z}_{AX,0} \\ \mathcal{Z}_{AX} &= \left(\frac{2\pi m k_B T}{h^2}\right) \cdot \left(\frac{\exp\left(h\nu_o/2k_B T\right)}{\exp\left(h\nu_o/k_B T\right)-1}\right) \exp\left(\frac{-E_{Cu/SiO_2}}{k_B T}\right) \end{aligned} \tag{5.3}$$

where ν_o is the vibration frequency of the bond between the adsorbed atom and the surface. According to [32] it can be estimated by

$$\nu_o = \frac{1}{2\pi}\sqrt{\frac{2\pi\epsilon r_o}{m\Delta^3}} \tag{5.4}$$

where ϵ is the adsorption energy, r_o= 2.35 $\times 10^{-10}$ meters is the bond length for Cu-Cu [31] and $r_o = 2.46\times10^{-10}$ meters for Cu-SiO_2 [30], and Δ^3 is the volume of the adsorbed species. This volume was estimated from the surface site density, $[\hat{X}]$, as $\Delta^3 = \left(1/[\hat{X}]\right)^{3/2}$. With these data the vibration frequencies for copper on copper and quartz substrates are, $\nu_o \approx 2\times10^{12}s^{-1}$ and $\nu_1 \approx 5\times10^{11}s^{-1}$, respectively.

For the surface site, in addition to the electronic ground state, $\mathcal{Z}_{X,0}$, there is a vibrational contribution commonly represented with a single frequency ν_1, which can be estimated from the adsorption energy using an equation similar to Equation 5.4 to be $5.278 \times 10^{11}\mathrm{s}^{-1}$ which makes the contribution $\mathcal{Z}_{X,vib} = 2.11$. Hence the partition function value of a surface site is given by

$$\mathcal{Z}_X = \mathcal{Z}_{X,vib}\mathcal{Z}_{X,0} = 2.11 \times \exp\left(\frac{-E_{SiO_2}}{k_B T}\right) \tag{5.5}$$

After applying the above considerations, Equation 5.1 transforms into

$$\frac{[AX]}{[A]\left([X]-[AX]\right)} = \frac{\mathcal{Z}_{AX,trans}}{\mathcal{Z}_{A,trans}\mathcal{Z}_{AX,vib}} \frac{\mathcal{Z}_{AX,0}}{\mathcal{Z}_{A,0}\mathcal{Z}_{X,0}}$$

and we have that $\theta_{AX} = [AX]/[\hat{X}]$ is the fraction of surface sites occupied with an atom from the gas phase. Using the ideal gas for $[A] = P_A/k_B T$ and the equations for the partition functions we obtain

$$\frac{\theta_{AX}}{1-\theta_{AX}} = \frac{P_A}{[\hat{X}]} \frac{h}{(2\pi m)^{1/2} (k_B T)^{3/2}} \left(\frac{\exp(h\nu_o/2k_B T)}{\exp(h\nu_o/k_B T) - 1} \right) \exp\left(\frac{-\epsilon_{Cu-SiO_2}}{k_B T} \right) \quad (5.6)$$

where h and k_B are Planck's and Boltzmann's constants, respectively. m is the mass of the atomic species being adsorbed. ϵ_1 is the adsorption energy which is the difference between the energies of the species in the separate and adsorbed state.

Now, if we define the adsorption equilibrium constant

$$K(T) = \frac{h}{\hat{X} (2\pi m)^{1/2} (k_B T)^{3/2}} \left(\frac{\exp(h\nu_o/2k_B T)}{\exp(h\nu_o/k_B T) - 1} \right) \exp\left(\frac{-\epsilon_1}{k_B T} \right) \quad (5.7)$$

Equation 5.6 becomes the Langmuir adsorption isotherm

$$\theta_{AX} = \frac{K(T) P_A}{1 + K(T) P_A}. \quad (5.8)$$

To calculate the fraction coverage of the surface by copper atoms we use Equation 5.8 and the appropriate adsorption energy ϵ_1 for each surface available for deposition, Cu and SiO_2. Then we use Equation 5.7 to calculate the fractional coverage of copper over a SiO_2 surface. The resulting adsorption isotherms are shown in Figure 5.3

From Figure 5.3 we observe that copper, as expected from the adsorption energy data in Chapter 4, is more likely to deposit on itself than on quartz. These calculations are used in Chapter 4 to estimate the adsorption isotherm constant, K_{ads}^{sp}, and fractional coverage, θ_{sp}, where $sp = Cu, CuI$, in equations 4.3 and 4.4.

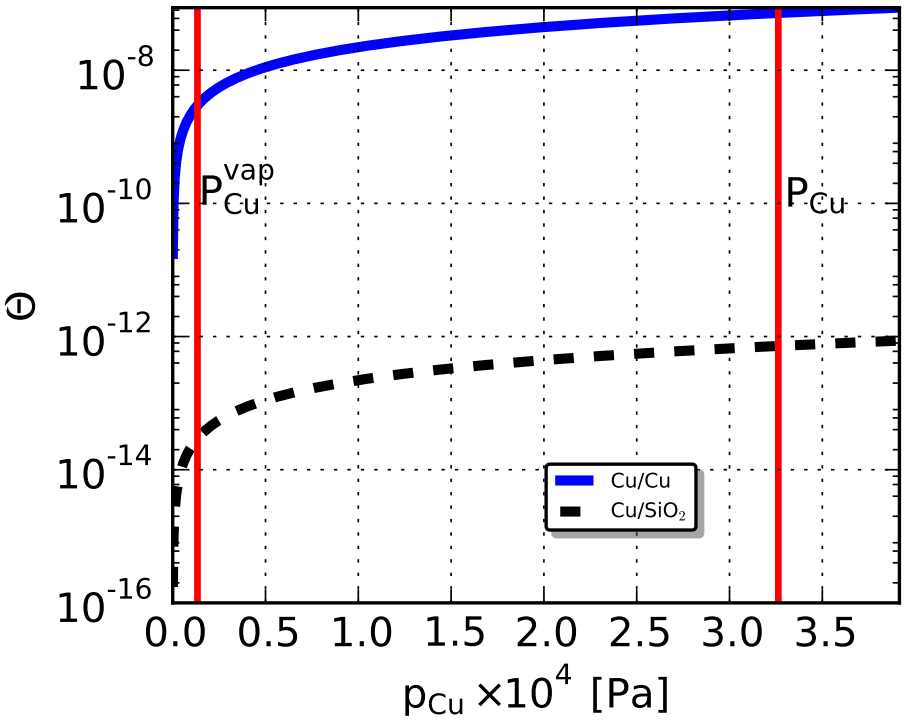

Figure 5.3: *Fractional coverage, θ, of copper on deposited copper and on a quartz substrate as a function of the partial pressure of copper in the gas phase. The red vertical lines indicate the copper partial pressure at the reactor temperature, $P_{Cu}^{va} = 0.133\times\ 10^{-4}$ Pa, and the copper partial pressure at which our reactor operates, $P_{Cu} = 4 \times 10^{-4}$ Pa.*

Chapter 6

Experimental deposition and image processing analysis of copper films

This appendix considers the chemical vapor deposition of copper using copper iodide as a precursor by the following reaction

$$\mathrm{CuI}(g) \rightarrow \mathrm{Cu}(s) + \frac{1}{2}\mathrm{I}_2(g)$$

in the hot wall tubular reactor sketched in Figure 4.1. The copper is deposited on quartz substrates and optical microscope images are obtained of the grown films. These images are digitally processed to estimate the size distribution of the copper clusters that form the film.

6.1 Experimental reactor system

The reactor system and much of the operating procedures for depositing Cu are the same as those described in Appendix A for the deposition of Cu_xO films. An schematic of the reactor is shown in Figure 4.1. Argon is used as a carrier gas and the copper iodide is fed in powder form in a ceramic boat to evaporate in the reactor and being carried downstream by the flow of Ar. The temperature settings for a typical CVD run in this system are in the range 725 - 775 °C . A calibrated rotameter gauge is used to control the Ar flow rate. While the reactor is heating to the desired temperature, the Ar carrier gas (fed to the annular inlet section where

the CuI boat is located) flow rate is set to a rotameter setting of 60 (570 sccm) to flush air from the process tube. This Ar flow is held constant through each experiment and the flow rate of 570 sccm is used for all experiments described in this appendix. Deposition takes place for 10 min, after which the reactor is allowed to cool under Ar carrier gas flow for another 10 min before the boat and substrate are removed. All deposition runs take place under atmospheric (total) pressure.

6.2 Results and analysis

6.2.1 Experimental island size distribution

The deposited films were visually examined under the optical microscope (Olympus CKX41 with a Photometrics Coolsnap EZ charge-couple device camera). The resulting image was later processed to have pixels of one color: white for the substrate and black for the copper molecules deposited.

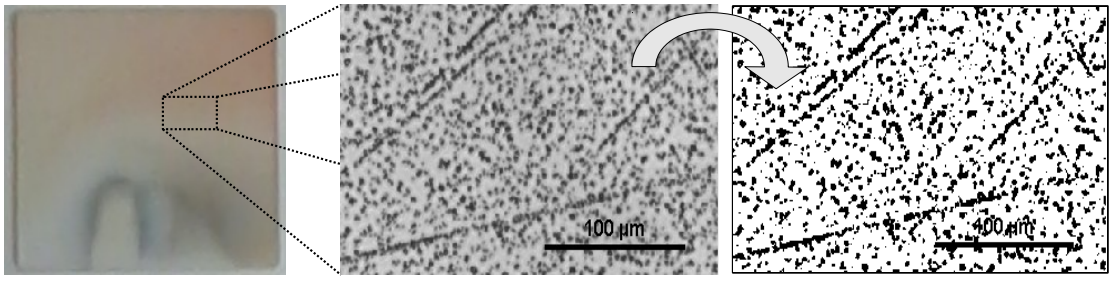

Figure 6.1: *Reproduction of Figure 4.2. The image on the left is a quartz substrate with copper deposited(red color), the image on the center is a microscope image of an zone in the substrate, and the image on the right is the black and white version of the microscope image. Details on the image analysis process are described in this section and also in the caption of 4.2*

The initial picture from the microscope had a RGB color format and was filtered through a numerical threshold of 127, which is the middle between black (0) and white (255), to eliminate noise in the image resulting in the black and white version shown in on the right of Figure 6.1 (which is a reproduction of Figure 4.2). The pixels in white are pixels from the substrate (SiO_2 which is transparent) while the black pixels indicate copper particles. The black and white images were processed using the *ndimage* tool from the *scipy* python library, to identify copper islands (clusters of black pixels) on the substrate.

The image on the right of Figure 6.1 shows that the deposited copper forms small islands with accumulation a clear tendency for copper crystals to grow along the film. This suggests that because of the weak bonding of copper with the SiO_2 surface, 0.1 eV, the copper deposited diffuses rapidly along the surface until it encounters another surface atom or cluster and sticks to it. The scratches on the substrate provide edge and kink sites of higher coordination where the copper adatoms are more likely to stick as observed in the figure. This concentration on the scratches and small size island distribution is considered to indicate that the dominant growth mechanism is the direct deposition of copper atoms on both surfaces. This would initially seem to contradict the results on the simulation in Chapter 4. However, this observation suggests that surface migration is important to provide the initial adsorbed copper atoms (on the kink sites generated by defects on the substrates surface) where the islands will grow during the deposition. It is then the growth of the island that is regulated by the direct deposition. In the simulation we assume that there are initially *nucSites* (see Table 4.2) on the quartz surface containing a

single copper atom where the islands will begin to grow during the deposition, in accordance with this experimental observations.

For this analysis, the islands are assumed to have a cubic structure since it is known that copper crystals have a FCC structure. Consequently the number of pixels of each island can be used to estimate the volume of the cubic island V_p. The volume of a cubic pixel converted to meters is

$$V_{m^3} = V_p \times c_{pix2m}^3 = 2.68 \times 10^{-19} \mathrm{m}^3$$

where $c_{pix2m} = 6.45 \times 10^{-7}$ m/pixel, is the conversion factor from pixel to micrometers obtained from the scale at which the camera was used. Finally the number of copper atoms in the island is estimated by $n_{Cu} = V_{m^3}/v_{Cu}$, where v_{Cu} is the atomic volume of copper. The histogram with the island size distribution is show in Figure 6.2.

6.2.2 Average side length analysis

This subsection presents an analysis to validate the the copper crystal size estimates. For this, the length of the deposition zone in the reactor (see Figure 4.1) was calculated using the results of the image analysis with a material balance. Table 6.1 summarizes the analysis of six image samples. Each sample was taken from a subsection of Figure 6.1, right, in such a manner to avoid scratched areas that would potentially bias the calculation of island size.

The results in Table 6.1 show that there are in average 1.275×10^{23} atoms in every square meter of the substrate, distributed in islands of side length of 1.704 micrometers. In the table, DepLen is the deposition length in the reactor that would

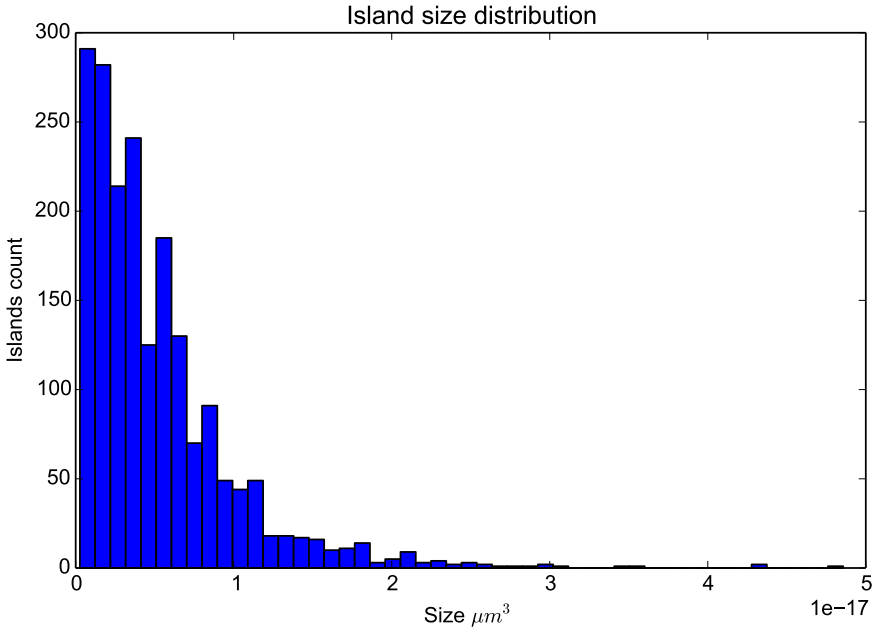

Figure 6.2: *Overall island size distribution. The size of the islands was estimated taking the pixel area as the base area of a cubic island.*

take to consume all the initial precursor and is estimated as follows

$$\mathsf{DepLen} = \frac{m^o_{CuI}}{MW_{CuI}} \frac{\rho_{Cu}}{2\pi R_o^2} \tag{6.1}$$

where $m^o_{CuI} = 0.1$ grams is the mass of precursor used in a deposition and $R_o = 1.91 \times 10^{-2}$m is the inner radius of the reactor tube. With these data, the average length of deposition along the reactor is about 19.7 centimeters, which is in good agreement with visual observations of deposition in the reactor supporting the assumption of cubic islands.

Table 6.1: *Analysis of image samples with a scale of 0.645 $\mu m/pixel$.*

Sample number	% pixel black/Total	$Cu_{total} \times 10^{15}$ $atoms$	$\rho_{Cu} \times 10^{23}$ $atoms/m^2$	DepLen cm	Image size $\mu m \times \mu m$	Side Length μm
1	15	2.18	1.11	22.4	116×168	1.76
2	18	3.24	1.37	18.1	141×167	1.93
3	17	2.25	1.30	19.1	110×156	1.67
4	14	0.95	1.07	23.2	88×100	1.70
5	19	1.96	1.39	17.9	92×151	1.60
6	19	0.72	1.41	17.6	54×95	1.55

% pixel = number of black pixels / total number of pixels in the image

Cu_{total} = total number of atoms in the image (total volume/Cu atom volume)

ρ_{Cu} = density of copper atoms in the image (total number of atoms in the image / image's area) $\left[atoms/m^2\right]$

DepLen = length of deposition in the reactor needed to consume 0.1 grams of copper iodide $[cm]$

Chapter 7

Conclusions and suggestions for future work

A model reduction methodology based on a Gauss-Jordan reaction factorization was developed in this thesis. The reaction factorization successfully identified the dominant dynamics of complex transport-reaction systems, tested the structural integrity of the kinetic mechanism considered in the system, and provides physical insight into quantities that are conserved in the system.

To identify the dominant dynamics, the factorization provided a rational approach to formulating standard singular perturbation representations of complex transport-reaction systems preserving the dominant dynamics of the original system. The factorization achieves these results by transforming the original composition coordinates into new reaction coordinates that are associated with each individual net-forward reaction rate to the maximum extent possible, i.e. by diagonalizing the reaction stoichiometry matrix. Even in the case where the diagonalization of the stoichiometry matrix was not fully realized, the singular perturbation problem was still valid and accomplished separation of time scales of the system in the outer solution.

The reaction factorization tested the structural integrity of the kinetic mechanism by recognizing redundant dynamics if they existed in the model; consequently, avoiding wasteful computations. Furthermore, the factorization revealed conserved

quantities in the new reaction coordinates it produced, such as conserved total number of atoms through the length of the tubular reactor described in Chapter 4.

A major contribution of this thesis was the formulation of the reaction factorization in a form suitable for application to dynamic, distributed-parameter reaction systems. For these systems, the factorization proved useful not only to separate the time scales of the system, but as a consequence it also provided a path rigorously decoupling the time evolution of the system and the spatial distribution so that two independent ordinary differential equation problems are to be solved rather than the original set of partial differential equations. Furthermore this approach solved the problem of how one formulates Danckwerts-type boundary conditions where gas-phase equilibrium reactions are important.

A series of object-oriented species classes was created to store molecular information in each species and structure statistical mechanics computations for absolute rate computations estimations of adsorption isotherms and deposition reaction rates. These classes have a broad application since they provide an organized way to automate calculations of fundamental rates that are required in a wide variety of multi-scale models such as alumina ALD [36].

A crystal growth model was proposed for the growth of copper films on quartz films at the microscopic level. This model was included in the Cu CVD plug flow model of Chapter 4. Using this model to track the average size (L) of copper islands growing on the film. The simulation results predicted the average island size that matches the experimental average size obtained from image processing of films Chapter 6 to be in the zone where the substrate is located in the reactor.

Finally, the effects of temperature and precursor flow on the composition of copper oxide films were statistically determined through a design of experiments and a subsequent surface response analysis of the digitized images of deposited films. Particularly for the amount of the two oxides, CuO and Cu_2O, present on the films.

Suggestions for future work

1 *Factorization of more detailed Cu and Cu_xO CVD processes.*

2 *Study of the modeling of 2D materials CVD.*

3 *Refinement of the film growth model.*

Project 1: Factorization of more detailed Cu and Cu_xO CVD processes

Future work should be extend the reaction factorization process to distributed CVD, which considers diffusive flux, since these systems are more realistic than the plug flow model described in Chapter 3. The application is very similar to the application in Chapter 4, the only difference is that the flux in this case contains the extra term of diffusion as opposed to only convection in the plug flow model.

The original model can be described by the following system of equations

$$\frac{\partial}{\partial t}\begin{bmatrix} [Cu_3I_3] \\ [I_2] \\ [Cu] \\ [CuI] \\ L \\ [Cu_2] \end{bmatrix} = \frac{\partial}{\partial \zeta}\begin{bmatrix} J_{Cu_3I_3} \\ J_{I_2} \\ J_{Cu} \\ J_{CuI} \\ 0 \\ J_{Cu_2} \end{bmatrix} + \begin{bmatrix} 1 & 0 & 0 & 0 & 0 & 0 \\ 0 & 1 & 0 & 0 & \sigma/2 & 0 \\ 0 & 2 & -2 & -\sigma & 0 & 0 \\ -3 & -2 & 0 & 0 & -\sigma & 0 \\ 0 & 0 & 0 & 0 & 0 & 1 \\ 0 & 0 & 1 & 0 & 0 & 0 \end{bmatrix}\begin{bmatrix} r_0 \\ r_1 \\ r_2 \\ r_3 \\ r_4 \\ r_5 \end{bmatrix}$$

where all the variables have the same meaning as in Chapter 4. $J_i = -\mathcal{D}_i \partial[i]/\partial\zeta - v[i]$ is the flux of species i, the kinetic expressions are given in Table 4.1, and the parameter for the simulation are the same from Table 4.2. In matrix form, the system becomes

$$\frac{\partial \mathbf{c}}{\partial t} = \frac{\partial \mathbf{J}}{\partial \zeta} + \mathbf{S} \cdot \mathbf{r}.$$

where $\mathbf{S}$ is the reaction stoichiometry matrix and the transformation matrix $\mathbf{U}$ that

diagonalizes it produces the new reaction coordinates

$$\mathbf{y} = \mathbf{U} \cdot \mathbf{c} = \begin{bmatrix} 1 & 0 & 0 & 0 & 0 & 0 \\ 0 & 1 & 0 & 0 & 0 & 0 \\ 0 & 0 & 0 & 0 & 0 & -2 \\ 0 & 2 & -1 & 0 & 0 & -2 \\ 0 & 0 & 0 & 0 & 1 & 0 \\ 3 & 2 & 0 & 1 & 0 & 0 \end{bmatrix} \cdot \begin{bmatrix} [Cu_3I_3] \\ [I_2] \\ [Cu] \\ [CuI] \\ L \\ [Cu2] \end{bmatrix} \tag{7.1}$$

$$\mathbf{y} = \mathbf{U} \cdot \mathbf{c} = \begin{bmatrix} [Cu_3I_3] \\ [I_2] \\ [Cu]_2 \\ 2\,[I_2] - [Cu] - 2\,[Cu_2] \\ L \\ 3\,[Cu_3I_3] + [CuI] + 2\,[I_2] \end{bmatrix} = \begin{bmatrix} z_0 \\ z_1 \\ z_2 \\ x_0 \\ x_1 \\ w_0 \end{bmatrix}$$

which allows us to write the system in the standard singular perturbation form shown below

$$\frac{\partial}{\partial t} \begin{bmatrix} z_0 \\ z_1 \\ z_2 \\ x_0 \\ x_1 \\ w_0 \end{bmatrix} = \frac{\partial}{\partial \zeta} \begin{bmatrix} J_{z_0} \\ J_{z_1} \\ J_{z_2} \\ J_{x_0} \\ 0 \\ J_{w_0} \end{bmatrix} + \begin{bmatrix} 1 & 0 & 0 & 0 & 0 & 0 \\ 0 & 1 & 0 & 0 & \sigma/2 & 0 \\ 0 & 0 & -2\sigma & 0 & 0 & 0 \\ 0 & 0 & 0 & \sigma & \sigma & 0 \\ 0 & 0 & 0 & 0 & 0 & 1 \\ 0 & 0 & 0 & 0 & 0 & 0 \end{bmatrix} \begin{bmatrix} \frac{1}{\epsilon_0} g_0 \\ \frac{1}{\epsilon_1} g_1 \\ \frac{1}{\epsilon_2} g_2 \\ f_3 \\ f_4 \\ \delta f_5 \end{bmatrix}$$

Letting $\epsilon_0, \epsilon_1, \epsilon_2 \to 0$ and $\delta \to 0$ produces the following semi-explicit DAE system

$$\begin{aligned} g_0 &= 0 \\ g_1 &= 0 \\ g_2 &= 0 \\ \frac{\partial J_{x_0}}{\partial \zeta} &= -\sigma f_3 - \sigma f_4 \\ \frac{\partial J_{x_1}}{\partial \tau} &= \delta f_5 \\ \frac{\partial J_{w_0}}{\partial \zeta} &= 0 \end{aligned} \tag{7.2}$$

which can be solved with a procedure similar to the one described in Chapter 3.

Once the application for the distributed Cu CVD system described above is completed, the next step should be consider the addition of the oxygen species and their pertinent reactions with the CuI system. This addition would not change the methodology for the application of the reaction factorization and can be solved to study the Cu_xO system that initialy motivated this research, for which previous experimental was presented in Appendix A.

Project 2: Study of the modeling of 2D materials CVD.

The island growth mechanism used to estimate the film growth in Chapter 4 can be modified to track the growth of two dimensional islands of different geometries. This modification enables the factorization in distributed CVD systems to be applied in the modeling of 2D materials growth that has shown potential for applications in electronic and optoelectronic devices [37].

Project 3: Refinement of the film growth model

Another direction for future work should be the refining of the film growth model to better track more properties of the film in time and space. For example a kinetic Monte Carlo (kMC) simulation model enables tracking not only of film thickness but also of surface roughness [38]. The use of a kMC simulation for the film growth increases the computational costs of the model. In this context the model reduction resulting from the reaction factorization can reduce considerably the computational costs.

An issue commonly encounter in these systems is the noise that the stochastic results of the kMC introduce on the macroscopic scale transport model. This noise can be decreased by using a filtering technique, e.g. a Kalman filter, on the kMC simulation. The resulting reduced model will be well suited to study the potential of using nanotubes as microreactors such as the ones in [39, 40, 41, 42].

Appendix A

Temperature and precursor influence in Cu_XO film growth and composition

In this appendix the deposition of Cu_2O and CuO by the reactions

$$CuI + \tfrac{1}{2}O_2 \rightarrow CuO(s) + \tfrac{1}{2}I_2$$

$$2CuI + \tfrac{1}{2}O_2 \rightarrow Cu_2O(s) + I_2$$

is considered. A set of experiments was carried out guided by a design of experiments to study the influence of temperature and precursor flux on the composition of copper oxide films grown in quartz substrates. The effect of these parameters was statistically determined with a surface response model analysis.

A.1 Reactor system and substrate preparation

The reactor system consists of a 3.8 cm ID cylindrical quartz process tube heated by a tube furnace (Fig. A.1). The digital furnace temperature controller allows time-programmed temperature profiles accurate to 1 °C. The inlet of the process tube has a custom-manufactured quartz fitting through which the argon (Ar) carrier and 19% O_2 in Ar precursor mixture are separately introduced into the reactor. Copper(I) iodide is used as the solid-source Cu precursor. Residual process gas is scrubbed in a chilled methanol bubbler to remove I_2 before being vented through the laboratory hood.

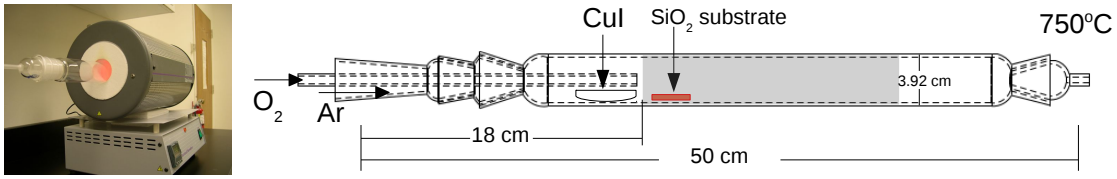

Figure A.1: *CuI CVD reactor process tube and furnace (left); schematic of CVD reactor showing relative positions of CuI precursor boat, O_2 mixture feed tube and substrate location.* $L_1 = 18cm$ *and* $L_2 = 32cm$.

A.1.1 Substrate preparation

The substrates used in this study are 2.54 cm $\times$ 2.54 cm square frosted quartz slides, 2.54 cm wide rectangles of pure copper sheets and ITO-coated glass. Before each run, the quartz substrates are soaked in a strong HCl solution overnight to remove previously deposited copper oxide films. Any oxides that remain after the acid treatment are removed with steel wool and repeated rinsing with acid. Copper substrates are prepared by roughening the surface with extra fine sandpaper; no preliminary preparation for the ITO-coated substrates was required. All three types of substrates then are rinsed with distilled water and methanol. Finally, the substrates are heated to 200 °C in air to dry.

A.1.2 Reactor operating procedure

Temperature settings for a typical CVD run in this system are in the range of 725 °C to 775 °C. Calibrated rotameter gauges are used to control the Ar and Ar/O_2 mixture flow rates. While the reactor is heating to the desired temperature the Ar carrier gas (fed to the annular inlet section where the CuI boat is located)

flow rate is set to a rotameter setting of 60 (570 sccm) to flush air from the process tube. This Ar flow is held constant through each experiment and the flow rate of 570 sccm is used for all experiments described in this paper. Before each deposition run, 0.1 g of the solid copper precursor (CuI) is measured into a ceramic boat; the boat is cleaned with a strong acid solution after every set of runs. When the reactor has reached the temperature set point the reactor is loaded first with the substrate, placed with its leading edge approximately $L_1 = 18$ cm into the reactor from the entrance collar, followed by the precursor boat containing CuI. The ceramic boat is placed upstream of the substrate in the zone swept by the Ar carrier gas (see Fig. A.1). The reactor tube then is sealed with the inlet gas fitting and the oxygen mixture flow rate is set to the desired rotameter setting. The 19% molar O_2 mixture flow rate corresponding to rotameter settings of $M = [5, 10, 15]$ are [4.9, 6.5, 8.1] sccm, respectively. Deposition takes place for 10 min, after which the reactor is allowed to cool under Ar carrier gas flow (no O_2 mixture) for another 10 min before the boat and substrate are removed. All deposition runs take place at atmospheric (total) pressure.

A.2 Representative films and design of experiments

In this study the effect of varying O_2 feed flow rates and reactor temperature on the deposition mechanism are explored. During the course of this study, the reactor was operated at three temperatures (725, 750, and 775 °C) and three argon/oxygen gas mixture flow rates (consisting of rotameter settings of 5, 10, or 15 at each of the

three temperatures). This set of nine experiments were repeated multiple times to collect sufficient data for statistical analysis.

A.2.1 Representative results

Figure A.2 shows representative samples of Cu_2O/CuO films produced in our reactor. Gas flow is from left to right in all cases shown. A striking feature of these films is the distinct separation between the Cu_2O (red) and CuO (black) film regions. Note that X-ray diffraction (XRD) analysis on samples taken from the each of the "visually apparent" (red vs. black) cuprous and cupric oxide regions *always* shows the presence of a single oxide phase. Furthermore, the films used for this modeling study were deposited on transparent substrates; visual inspection of each film revealed identical spatial patterns for the initial and final growth surfaces of CuO/Cu_2O films. Details of the film analysis are reported in Levine[43].

Figure A.2-A shows an increasing fraction of Cu_2O from left to right—these experiments correspond to a decreasing sequence of O_2 mixture flow rates. Figure A.2-B displays a pure Cu_2O film deposited on a Cu substrate, produced under reactor operating conditions that would otherwise deposit a Cu_2O/CuO film on a quartz substrate. Significant differences also were observed in films grown on the ITO-coated/bare sides of the ITO-coated glass substrates [44]. It is this strong substrate dependency that suggests the predominant role the nucleation and/or surface reactions play and that motivate the experiments and analysis that follow.

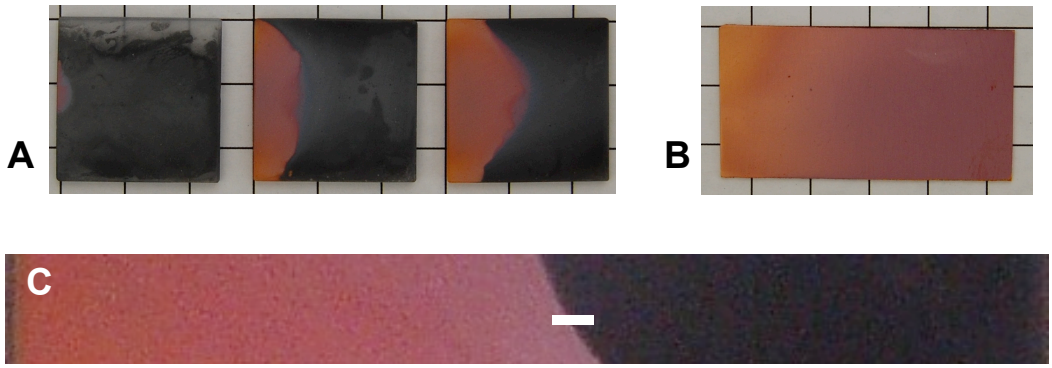

Figure A.2: *Cu_2O/CuO deposition on quartz (A); O_2 mixture flows for the three samples are $M = 60$ (left), 30 (center), and 20 (right). Cu_2O on Cu substrate is shown as (B) corresponding to $M = 30$ O_2 mixture flow. The grid shown in the background of A and B corresponds to 1 cm spacing. Image (C) illustrates the sharpness of the transition between the films; the horizontal white bar corresponds to 1 mm. This film was deposited with $M = 15$. For all cases, deposition was performed at $T = 750\ ^\circ C$.*

A.2.2 Design of experiments

The effect of varying the reactor temperature T and oxygen mixture flow meter setting M was investigated. A three-level full factorial experiment design was created for the two factors T and M; factor values are listed in Table A.1. The two factors are scaled by subtracting the nominal operating conditions and dividing the difference by the maximum deviation used in the three-level design:

$$m = \frac{M - 10}{5}, \qquad t = \frac{T - 750\ ^\circ\mathrm{C}}{25\ \mathrm{K}}.$$

The scaled factors are represented in vector form as $\mathbf{x} = [m\ t]^T$.

Information regarding the $n_M = 9$ sets of experimental conditions were loaded into a vector of MATLAB `paramdata` objects. Each object includes measured variable (% cuprous oxide) and the two parameter (factor) names and values; the data

M	T (°C)	m	t	precursor Cu/O ratio	no. exp.	Y (% Cu_2O)	y_{RSM} (reduced)	y_{1D}
15	725	1	-1	0.9	3	27.6	27.1	43.7
15	750	1	0	1.2	2	39.5	35.6	64.1
15	775	1	1	1.6	3	31.9	43.9	83.1
10	725	0	-1	1.1	3	37.7	45.9	48.4
10	750	0	0	1.5	9	62.2	54.2	68.6
10	775	0	1	2.0	4	78.5	62.5	87.4
5	725	-1	-1	1.5	3	70.2	64.5	54.4
5	750	-1	0	2.0	5	65.6	72.8	74.4
5	775	-1	1	2.6	3	74.8	81.1	92.9

Table A.1: *Experimental conditions defined by a three-level, full factorial design for the two factors T and M (dimensionless rotameter setting), their normalized values t and m, and the corresponding measured values for film % Cu_2O. The Cu/O ratios correspond to molar values of the atomic species. The fourth column from the right reports the number of runs performed under each set of operating conditions; remaining columns give measured Y, empirical y_{RSM}, and 1-dimensional transport model predictions y_{1D} of film Cu_2O%.*

structures developed by Leon [45, 46] provide a convenient means of storing the parameterized data, sorting and manipulating the data, and constructing response surface models from selected sets of data.

A.2.3 Image analysis

Given the large number (35 in total) of experiments that were performed[1], a rapid method for estimating the ratio of Cu_2O to CuO over the entire substrate was required; because of the nature of the deposition reaction and precursor transport modeling found later in this analysis, direct measurement of film thickness was not required. Based on the distinct color difference between the oxide phases and owing to the sharpness of the boundary between them, a computational image-processing approach was developed to characterize the films.

In our approach, a high-resolution color photograph of each film was read into a MATLAB image object and was then converted from an RGB to grayscale image. Histograms of each grayscale image clearly showed a bimodal distribution in the gray shade distribution (Fig. A.3), with the two peaks corresponding to the two copper oxide phases. The corresponding pixels of each phase then were reset to a binary distribution, resulting in the sharply contrasting phases shown in Fig. A.3; the relative proportions of each phase were determined by simply counting the number of each of the two pixel values. Experiments corresponding to identical factor values were averaged, to give the $n_M = 9$ Cu_2O percentages shown in Fig. A.3 and in Table A.1.

[1]Repeated experiments were averaged to give $n_M = 9$.

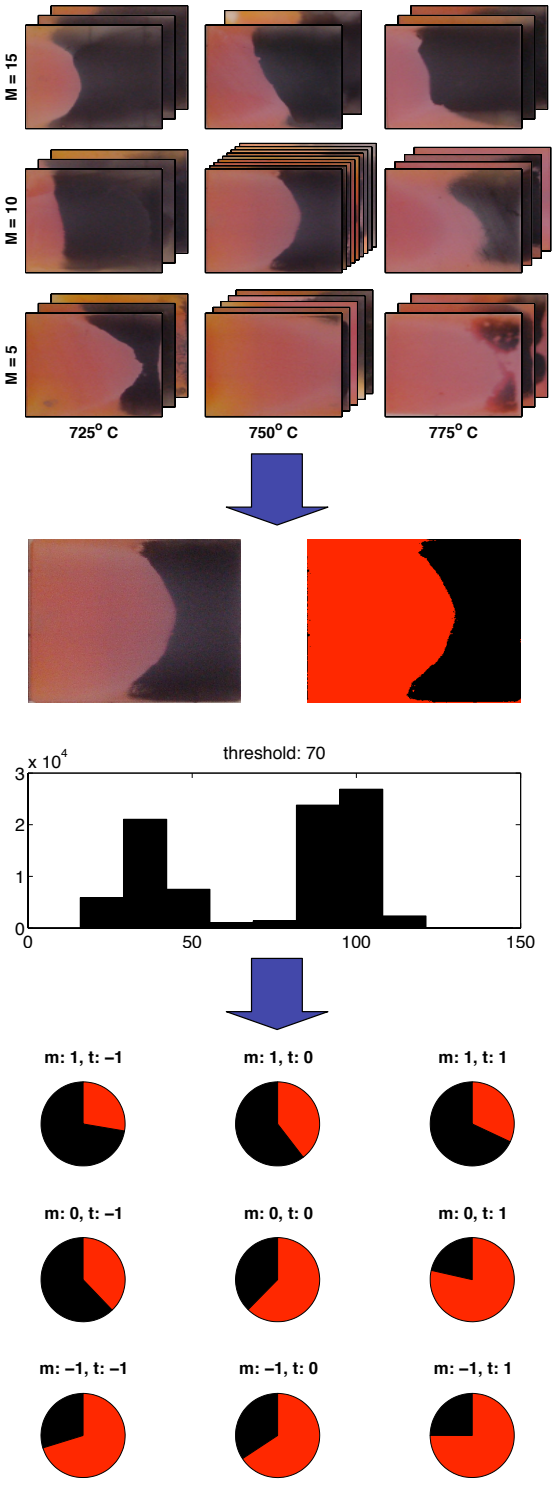

Figure A.3: *The image processing approach to determining film composition from original film images (top). Note the bimodal distribution in the histogram (center), indicating the fraction of each form of the copper oxide. Pie charts at the bottom indicate relative ratios of* Cu_2O *(red) and CuO (black).*

A.3 Response surface modeling

Given the column vector form of $\mathbf{x}$, we can write the unknown function f that results in the measured value $Y = f(\mathbf{x}) + \epsilon$ and a quadratic response surface model that predicts measurement value as

$$y = b_0 + [\mathbf{b}]^T \mathbf{x} + \mathbf{x}^T \mathbf{B} \mathbf{x} \tag{A.1}$$

where Y denotes the measured percentage of cuprous oxide in the sample, y is the corresponding prediction of the cuprous oxide percentage, and ϵ represents measurement error.

In the model (A.1), b_0 is a scalar corresponding to the expected value of Y at the nominal operating conditions, and $\mathbf{b}^{2\times1}$ is a vector and $\mathbf{B}^{2\times2}$ a matrix of model coefficients to be determined from the data contained in Table A.1. To see this more clearly, we can write the model as

$$y = b_0 + b_1 m + b_2 t + B_{1,1} m^2 + B_{1,2} mt + B_{2,2} t^2$$

From the equation above we can see that element $B_{2,1}$ is not used and can be set to zero.

A response surface model of the form (A.1) is identified using the data in Table A.1, producing a set of coefficients $\{b_0, \mathbf{b}, \mathbf{B}\}$. From the discussion above, we see there are $1 + 2 + 3 = 6$ b_0, $\mathbf{b}$, and $\mathbf{B}$ coefficients to identify in (A.1) from the $n_M = 9$ data points. Reordering the coefficients into a single column vector $\mathbf{c}^{6\times1}$ and using the vector of measurement data $\mathbf{Y}$, the resulting regression problem can be written as $\mathbf{Y} = \mathbf{X}\mathbf{c}$ where $\mathbf{X}^{n_M\times6}$ is a rectangular array constructed by the factor

		full model		reduced model	
model coeff	vector name	value	std error $s_{b,k}$	value	std error $s_{b,k}$
b_0	c_1	61.0	9.93	54.2	3.52
b_1	c_2	-18.6	5.44	-18.6	4.31
b_2	c_3	8.30	5.44	8.30	4.31
$B_{1,1}$	c_4	-7.88	9.42	0	0
$B_{1,2}$	c_5	-0.09	6.66	0	0
$B_{2,2}$	c_6	-2.32	9.42	0	0
R^2		0.8313		0.7887	
σ_M		13.3		10.5	

Table A.2: *Model coefficients for the full and reduced response surface models.*

values (and all of the relevant products m^2, mt, and t^2) of the n_M experiments. Having more equations than unknowns, the least squares technique is used to find the optimal set of model coefficients $\mathbf{c} = [\mathbf{X}^T\mathbf{X}]^{-1}\mathbf{X}^T\mathbf{Y}$. This least-squares solution gives the model coefficients listed in Table A.2.

A.3.1 Analysis of the full model

With our model in hand, we turn to assessing its validity with the main goal being identification and removal of model terms that are statistically irrelevant. To begin, using the data contained in Table A.1, we quantify the total variation in the measured data Y by computing the total sum of squares $SST = \sum_{i=1}^{n_M}(Y_i - \bar{Y})^2 = 3159$ where $\bar{Y}$ is the mean measured value of the modeling data set. The variability

not captured by the full model is defined by the sum of squared residuals $SSE = \sum_{i=1}^{n_M}(Y_i - y_i)^2 = 533$ where y_i is the predicted value of the measured value computed using the factor values corresponding to measurement Y_i. These quantities can be used immediately to compute the coefficient of determination

$$R^2 = 1 - \frac{SSE}{SST} = 0.8313$$

indicating a reasonably good fit to the modeling data. The variance of the modeling error then is approximated by

$$\sigma_M^2 \approx \frac{SSE}{n_M - p} = 178 \quad \text{and} \quad \sigma_M = 13.3$$

where $n_M = 9$ is the number of data points and $p = 6$ the number of identified parameters in the model.

These data are used to create Fig. A.4, where the model predictions are compared to the true values; if the model predictions were perfect, all of the blue circles (modeling data) would line up on the diagonal line. The σ_M are plotted as red dashed lines in Fig. A.4. Because of the relatively large value of R^2 and that most of the predictions lie inside $\pm\sigma_M$, which allows us to conclude that the model accuracy is reasonable for the identified response surface model (RSM).

A.3.2 Reduced model

Because of the assumption that parameter estimate errors are normally distributed with zero mean, we can compute the approximations $s_{b,k}^2$ to the true parameter variance $\sigma_{b,k}^2$ to assess the accuracy of our b_i and $B_{i,j}$. These variances are listed (in terms of standard error) in Table A.2 and are computed as

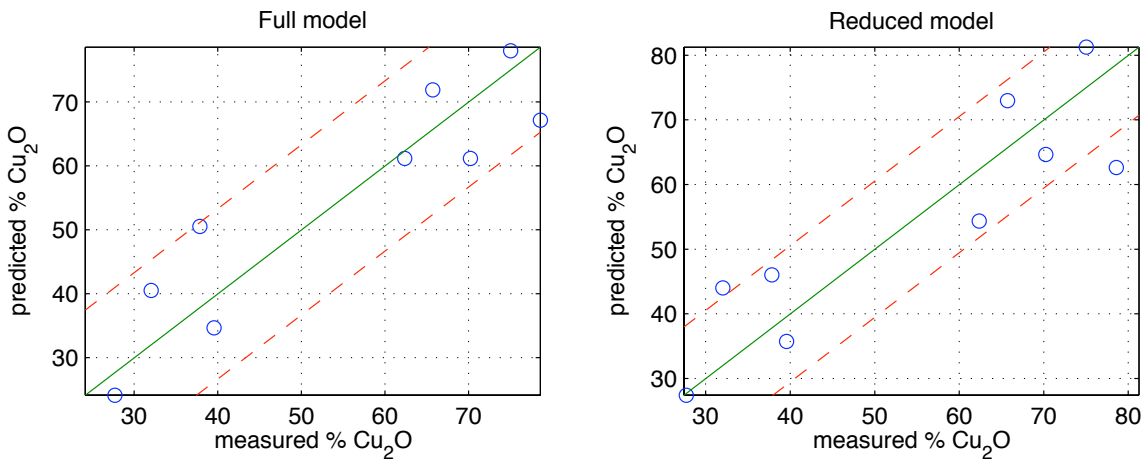

Figure A.4: *Full model predictions for film composition (left) and the reduced model (right) compared to modeling (blue circles) data; dashed red lines indicate* $\pm\sigma_M$.

$\sigma^2_{b,k} \approx s^2_{b,k} = [\mathbf{X}^T\mathbf{X}]^{-1}_{k,k}\sigma^2_M$ where the k, k subscripts denote diagonal elements of $[\mathbf{X}^T\mathbf{X}]^{-1}$. The ratio of each estimated parameter standard deviation $s_{b,k}$ and the parameter value gives some feel for which parameters may be of questionable validity. This evaluation process is formalized using Student's t-test whereby the t-values for each coefficient are first computed as $t_k = (c_k - 0)/s_{b,k}$ and then used as a test of whether the coefficient can be statistically distinguished from zero. We then select a parameter confidence level; in this case we wish to determine which parameters we are 75% ($\alpha = 0.25$) sure are actually non-zero. Using the MATLAB function `tinv`, we compute $t_{\alpha/2,dof}$ and flag all parameters falling outside $-t_{\alpha/2,dof} < t_k < t_{\alpha/2,dof}$. The degrees of freedom in this case $dof = 9 - 6 = 3$, and so $t_{0.125,3} = 1.42$.

Removing the terms that cannot be distinguished from zero by this test and recomputing the remaining parameter values using the modeling data set results in a reduced model predicting the Cu_2O percentage y as a function of the two input

factors

$$y = b_0 + b_1 m + b_2 t \tag{A.2}$$

with parameter values tabulated in Table A.2. As with the full model, the reduced model predictions and true measurements are compared in Fig. A.4, where it can be seen that while there is a bit more spread in the predictions relative to the σ_M error bars, the model compares well to the measured data. Furthermore, we find the coefficient of determination R^2 of the reduced model changes only slightly between the full and reduced models.

Given the relative simplicity of the reduced model, two important trends become clear for this CVD system:

1. Given the negative value of b_1 the amount of Cu_2O relative to CuO will **decrease** with increasing O_2 flow at the nominal operating point, an observation that makes physical sense based solely on the stoichiometry of the film phases;

2. Because b_2 is positive, the amount of Cu_2O relative to CuO will **increase** with increasing temperature at the nominal operating point, an observation consistent with Ottosson and Carlsson [9] and with Yoon *et al.* [47] where Cu_2O/CuO films were deposited by ion beam sputtering in an O_2 environment. Interestingly, this trend is *opposite* to that reported by Barreca *et al.* [10] and Condorelli *et al.* [48] for MOCVD systems.

Appendix B

Derivation of discretization weights

This appendix illustrates the derivation of the discretization weights for the finite differences of the first and second derivatives used in Chapter 4.

B.1 Second order accuracy Taylor's expansion

To approximate the first and second derivatives with respect to ζ of a function f with values defined at three interior collocation points ζ_{i-1}, ζ_i and ζ_{i+1} we use a the Taylor's series expansion approximation of f around ζ_i for the other two points given by the equations:

$$\begin{aligned} f_{i-1} &= f_i + f_i' \left(\zeta_{i-1} - \zeta_i\right) + \tfrac{1}{2} f_i'' \left(\zeta_{i-1} - \zeta_i\right)^2 \\ f_{i+1} &= f_i + f_i' \left(\zeta_{i+1} - \zeta_i\right) + \tfrac{1}{2} f_i'' \left(\zeta_{i+1} - \zeta_i\right)^2 \end{aligned} \tag{B.1}$$

for simplicity in the following derivation we let $\Delta\zeta_{i+1} = \zeta_{i+1} - \zeta_i$ and $\Delta\zeta_{i-1} = \zeta_{i-1} - \zeta_i$.

B.1.1 Finite differences of first and second dervatives

To find the discretization weights for the first derivative, we solve the second equation in (B.1) for f_i'', and substitute in the first equation to obtain

$$f_i' = \frac{\Delta\zeta_{i+1}^2}{\xi_i} f_{i-1} + \frac{\Delta\zeta_{i-1}^2 - \Delta\zeta_{i+1}^2}{\xi_i} f_i - \frac{\Delta\zeta_{i-1}^2}{\xi_i} f_{i+1} \tag{B.2}$$

where

$$\xi_i = \Delta\zeta_{i-1}\Delta\zeta_{i+1}^2 - \Delta\zeta_{i+1}\Delta\zeta_{i-1}^2$$

In a similar manner, to find the discretization weights for the second derivative, we solve the second equation for f_i'' in (B.1) and substitute in the first equation to obtain

$$f_i'' = \frac{\Delta\zeta_{i+1}}{\xi_{2i}} f_{i-1} + \frac{\Delta\zeta_{i-1} - \Delta\zeta_{i+1}}{\xi_{2i}} f_i - \frac{\Delta\zeta_{i-1}}{\xi_{2i}} f_{i+1} \tag{B.3}$$

where

$$\xi_{2i} = \frac{\Delta\zeta_{i+1}\Delta\zeta_{i-1}^2 - \Delta\zeta_{i-1}\Delta\zeta_{i+1}^2}{2}$$

At the lower bound of the interval we cannot use a centered finite difference, and so we use the values of ζ_2 and ζ_3 to compute the Taylor series expansion at ζ_1 and we find

$$f_1' = \frac{(\zeta_2 - \zeta_1)^2 - (\zeta_3 - \zeta_1)^2}{\xi_1} f_1 + \frac{(\zeta_3 - \zeta_1)^2}{\xi_1} f_2 - \frac{(\zeta_2 - \zeta_1)^2}{\xi_1} f_3 \tag{B.4}$$

where

$$\xi_1 = (\zeta_2 - \zeta_1)(\zeta_3 - \zeta_1)^2 - (\zeta_3 - \zeta_1)(\zeta_2 - \zeta_1)^2$$

Finally at the upper bound of the interval (collocation point N), we have

$$f_N' = \frac{(\zeta_{N-1} - \zeta_N)^2 - (\zeta_{N-2} - \zeta_N)^2}{\xi_N} f_{N-2} + \frac{(\zeta_{N-2} - \zeta_N)^2}{\xi_N} f_{N-1} - \frac{(\zeta_2 - \zeta_1)^2}{\xi_N} f_N \tag{B.5}$$

where

$$\xi_N = (\zeta_{N-1} - \zeta_N)(\zeta_{N-2} - \zeta_N)^2 - (\zeta_{N-2} - \zeta_N)(\zeta_{N-1} - \zeta_N)^2$$

Bibliography

[1] Brian G. Willis and David V. Lang. Oxidation mechanism of ionic transport of copper in Sio_2 dielectrics. *Thin Solid Films*, 467:284–293, 2004.

[2] I. A. Rauf, R. Siemsen, M. Grunwell, R. F. Egerton, and M. Sayer. Gas-phase nucleation during chemical vapor deposition of copper films and its effect on the resistivity of deposited films. *Journal of Materials Research*, 14(11):4345–4350, 1999.

[3] NIki S., Contreras M., Repins I., Powalla M., Kushiya K, Ishizuka S., and Matsubara K. Cigs absorbers and processes. *Progress in Photovoltaics: Research and Applications*, 18:453–466, 2010.

[4] Maengjun Kim and SungHo Lee SangHo Sohn. Reaction pathways for copper indium diselenide thin film formation from single multiple InSe/CuSe bilayer stacks. *Thin Solid Films*, 531:125–130, 2013.

[5] R. A. J. Shelton. Vapour pressures of the solid copper(i) halides. *Transactions of the Faraday Society*, pages 2213–2218, 1961.

[6] R. A. J. Shelton. Vapour-phase deposition of copper by the iodide process. *Transactions of the Faraday Society*, 62:222–228, 1966.

[7] W. M. Keeffe. Recent progress in metal halide discharge-lamp research. *IEE PROC.*, 127:191–189, 1980.

[8] L. S. Hong and H. Komiyama. Chemical vapor deposition of cuox films by cui and o2: Role of cluster formation on film morphology. *J. Am. Ceram. Soc.*, 74:1597, 1991.

[9] Mikael Ottosson and Jan-Otto Carlsson. Chemical vapour deposition of Cu_2O and CuO from CuI and O_2 or N_2O. *Surface and Coatings Technology*, 78:263–273, 1996.

[10] D. Barreca, P. Fornasiero, A. Gasparotto, C. Maccato, V. Gombac, and E. Tondello. The Potential of Cu_2O and CuO Nanosystems on the Photocatalytic H_2 Production. *ChemSusChem*, 2:230, 2009.

[11] Yatendra S. Chaudhary, Anshul Agrawal, Rohit Shrivastav, Vibha R. Satsangi, and Sahab Dass. A study on the photoelectrochemical properties of copper oxide thin films. *Internation Journal of Hydrogen Energy.*, 29:131–134, 2004.

[12] P. E. DeJongh, D. Vanmaekelbergh, and J. J. Kelly. Photoelectrochemistry of Electrodeposited Cu_2O. *Journal of the Electrochemical Society*, 147:486, 2000.

[13] Ryoki Nomura, Yasuharu Seki, and Haruo Matsuda. Preparaton of $CuinS_2$ thin films by single-source MOCVD process using $Bu_2In(SPr)Cu(S_2CNPr^i_2)$. *J. Mater. Chem.*, 2(7):765–766, 1992.

[14] D. Arana Chavez, E. Toumayan, F. Lora, C. McCaslin, and R. A. Adomaitis. Modeling the transport and reaction mechanisms of copper oxide. *CVD. Journal of Chemical Vapor Deposition.*, 16:336–345, 2010.

[15] U. Maas and S.B. Pope. Simplifying chemical kinetics: Intrinsic low-dimensional manifolds in composition space, 1992.

[16] S. H. Lam and D. a. Goussis. The CSP method for simplifying kinetics. *International Journal of Chemical Kinetics*, 26(4):461–486, 1994.

[17] M. Hadjinicolaou and D. A. Goussis. Asymptotic solution of stiff PDEs with the CSP method: The reaction diffusion equation. *SIAM J. SCI COMPUT.*, 20(3):781–810, 1999.

[18] Aditya Kumar, Panagiotis D. Christofides, and Prodromos Daoutidis. Singular perturbation modeling of nonlinear processes with nonexplicit time-scale multiplicity. *Chemical Engineering Science*, 53(8):1491–1504, 1998.

[19] Nishith Vora and Prodromos Daoutidis. Nonlinear Model Reduction of Chemical Reaction Systems. *AIChE Journal*, 47(10):2320–2332, 2001.

[20] Marie Nathalie Contou Carrere and Prodromos Daoutidis. Model reduction and control of multi-scale reaction-convection processes. *Chemical Engineering Science*, 63:4012–4025, 2008.

[21] L T Biegler. Differential-Algebraic Equations (DAEs). pages 1–40, 2000.

[22] Michael Baldea and Prodromos Daoutidis. Model reduction and control of reactor-heat exchanger networks. *Journal of Process Control*, 16(3):265–274, 2006.

[23] S. S. Sujit, A. I. Torres, and P. Daoutidis. Networks with large solvent recycle: Dynamics, hierarchical control, and a biorefinery application. *AIChE Journal*, 58:1764–1777, 2011.

[24] Ali Hasan Nayfeh. *Introduction to Perturbation Techniques*. John Wiley and Sons, 1981.

[25] R. C. Vieira and E. C. Biscaia. Direct methods for consistent initialization of DAE systems. *Computers and Chemical Engineering*, 25(9-10):1299–1311, 2001.

[26] D. E. Schwarz. Consistent initialization for DAEs in Hessenberg form. *Numerical Algorithms*, 52(4):629–648, 2009.

[27] Constantinos C. Pantelides. The consistent initialization of differential-algebraic systems. *SIAM J. Sci. Stat. Comput.*, 9:213–231, 1988.

[28] U. Mass and S.B. Pope. Simplifying Chemical Kinetic: Intrinsic Low-Dimensional Manifolds in Composition Space. *COMBUSTION AND FLAME*, 88:239–264, 1992.

[29] Diana Estevez Schwarz. Consistent initialization for DAEs in Hessenberg form. *Numer Algor*, 52:629–648, 2009.

[30] Nuria Lopez, Francesc Illas, and Gianfranco Pacchioni. Ab Initio Theory of Metal Deposition on SiO_2. 1. Cu_n ($n = 1 - 5$) Clusters on Nonbridging Oxygen Defects. *J. Phys. Chem. B*, 103:1712–1718, 1999.

[31] Perla B. Balbuena, Pedro A. Derosa, and Jorge M. Seminario. Dsensity Functional Theory Study of Copper Clusters. *J. Phys. Chem. B*, 103:2830–2840, 1999.

[32] K. J. Laidler, S. Glasstone, and H. Eyring. Application of the Theory of Absolute Reaction Rates to Heterogeneous Processes I. The Adsorption and Desorption of Gases. *Journal of Chemical Physics*, 8:659–667, 1940.

[33] Stanley I. Sandler. *An Introduction to Applied Statistical Thermodynamics*. John Wiley and Sons, Inc, 2011.

[34] Terrell L. Hill. *An Introduction to Statistical Thermodynamics*. Dover Publications, Inc., 1986.

[35] NIST Computational Chemistry Comparison and Benchmark Database NIST Standard Reference Database Number 101 Release 16a, August 2013, Editor: Russell D. Johnson III http://cccbdb.nist.gov/.

[36] Elizabeth M. Remmers. *Master Thesis:* Ab initio determination of kinetics for atomic layer deposition mode. Master's thesis, University of Maryland, 2015.

[37] Xingli Wang, Yongji Gong, Gang Shi, Wai Leong Chow, Kunttal Keyshar, Gonglan Ye, Robert Vajtai, Jun Lou, Zheng Liu, Emilie Ringe, Beng Kang Tay, and Pulickel M. Ajayan. Chemical Vapor Deposition Growth of Crystalline Monolayer $MoSe_2$. *ACS Nano*, 8(5):5125–5131, March 2014.

[38] Yiming Luo and Panagiotis D. Christofides. Estimation and control of surface roughness in thin film growth using kinetic monte carlo model. *Chemical Engineering Science*, 58(14):3115–3129, 2003.

[39] Hitoshi Ogihara, Sakae Takenaka, Ichiro Yamanaka, Eishi Tanabe, Akira Genseki, and Kiyoshi Otsuka. Synthesis of SiO2 nanotubes and their application as nanoscale reactors. *Chemistry of Materials*, 18(4):996–1000, 2006.

[40] Sy Lee and Ky Choi. Polymerization of Ethylene over rac-Et (1-indenyl) 2ZrCl2/MAO Catalyst Supported on Pseudo-Inverse Opal Silica Particles. *Industrial & Engineering Chemistry Research*, 51(29):9742–9749, 2012.

[41] Sang Yool Lee, Sung Kyoung Kim, Thao M. Nguyen, Jin Suk Chung, Sang Bok Lee, and Kyu Yong Choi. Kinetics of styrene polymerization to syndiotactic polystyrene over metallocene catalyst on flat surface, silica nanotube reactors and porous silica particles. *Macromolecules*, 44(6):1385–1392, 2011.

[42] Joong Jin Han, Sang Yool Lee, Sang Bok Lee, and Kyu Yong Choi. Silica Nanotube Reactors for Catalytic Polymerization of Styrene and Olefins. *Macromolecular Symposia*, 289(1):25–32, 2010.

[43] R. Levine and R. A. Adomaitis. ISR Technical Report. Technical report, Unpublished, 2010.

[44] G. Guglietta, T. Wanga, R. Pati, S. Eherman, and R. A. Adomaitis. Solar Hydrogen and Nanotechnology IV. In Frank E. Osterloh, editor, *Proc. of SPIE*, Bellingham, WA, 740807-1, 2009. SPIE.

[45] M. P. Leon. Full Wafer Map Response Surface Models for Combinatorial Chemical Vapor Deposition Reactor Operations *m.s. dissertation*. M.S. Dissertation, University of Maryland, 2008.

[46] M. P. Leon and R. A. Adomaitis. Full-wafer mapping and response surface modeling ttechnique for thin film deposition processes. *J. Crystal Growth*, 311(13):3399–3408, 2009.

[47] K. H. Yoon, W. J. Choi, and D. H. Kang. Photoelectrochemical properties of copper oxide thin films coated on an n-Si substrate. *Thin Solid Films*, 372(1-2):250–256, 2000.

[48] Guglielmo G. Condorelli, Graziella Malandrino, and Ignazio L. Fragala. Kinetic study of MOCVD fabrication of Copper(I) and Copper(II) oxide films. *Chemical Vapor Deposition*, 5(1):21–27, 1999.

Papers

- Arana-Chavez D., Toumayan E., Lora F., McCaslin C., Adomaitis R.A. Modeling the Transport and Reaction Mechanisms of Copper Oxide CVD. *Journal of Chemical Vapor Deposition* Vol **16** 2010, 336-345.

Presentations

- Arana-Chavez D. and Adomaitis R. A. Chemical Vapor Deposition of Copper: Study of Gas Phase Nucleation. AIChE Annual Meeting. San Francisco, California, November 3-8, 2013.

- Arana-Chavez D. and Adomaitis R. A. Modelling spatial variations of copper oxide thin film deposition. ChBE / CHEM / MSE Research Festival. University of Maryland at College Park, March 2012.

- Arana-Chavez D. and Adomaitis R. A. Modeling Chemical Vapor Deposition of Copper Oxide Films for Solar Energy Applications and Hydrogen Production. SACNAS National Conference. San Jose, California, October 26-30, 2011.

- Arana-Chavez D. and Adomaitis R. A. Modeling Spatial Variations In Thin-Film Processing of Copper Oxide Films for Solar Energy Applications and Hydrogen Production. AIChE Annual Meeting. Minneapolis, Minnesota, October 16-20, 2011.

- Dwivedi, V. D. Arana-Chavez, and R. A. Adomaitis Multiscale Simulation and Optimization of an Atomic Layer Deposition Process in a Nanoporous Material, Paper 140d 2009 AIChE Annual Meeting, Nashville, TN.